








Research Article

In Situ Sol-Gel Assembly of Graphitic Carbonitride Nanosheet-Supported Colloidal Binary Metal Sulfide into Nanosandwich-Like Multifunctional 3D Macroporous Aerogel Catalysts for Asymmetric Supercapacitor and Electrocatalytic Oxygen and Hydrogen Evolution

Vinayak G. Parale ¹, Younghun Kim ¹, Varsha D. Phadtare ¹, Taehee Kim ¹,
Haryeong Choi ¹, Umakant M. Patil ^{1,2} and Hyung-Ho Park ¹

¹Department of Materials Science and Engineering, Yonsei University, 50 Yonsei-ro, Seodaemun-gu, Seoul 03722, Republic of Korea

²Center for Interdisciplinary Research, D. Y. Patil Education Society (Deemed to be University), Kasaba Bawada, Kolhapur 416 006, India

Correspondence should be addressed to Hyung-Ho Park; [hhpark@yonsei.ac.kr](mailto:hypark@yonsei.ac.kr)

Received 31 May 2023; Revised 14 July 2023; Accepted 30 November 2023; Published 19 December 2023

Academic Editor: Kisan Chhetri

Copyright © 2023 Vinayak G. Parale et al. This is an open access article distributed under the Creative Commons Attribution License, which permits unrestricted use, distribution, and reproduction in any medium, provided the original work is properly cited.

It is challenging to develop scalable and stable multifunctional catalysts for energy storage and conversion applications. To address the above challenges, we designed 3D macroporous nanosandwich-like aerogels using an in situ sol-gel assembly for 2D g-C₃N₄ nanosheet-supported NiCo₂S₄ nanoporous aerogels. The resultant in situ method not only assembles NiCo₂S₄ but also 2D g-C₃N₄ into the sandwich-like 3D network, allowing rapid ion and electron transport. The potential of g-C₃N₄ and NiCo₂S₄ in electrochemical energy storage and electrocatalysis is promising for improving its electrochemical activities. The synthesized 3D NiCo₂S₄/g-C₃N₄ (3%) composite aerogel electrode achieved a remarkable specific capacitance value, 1083 F·g⁻¹ at 5 mA·cm⁻² current density with 87.03% cyclic stability. Furthermore, the asymmetric electrochemical supercapacitor device was fabricated with a maximum specific energy of 43 Wh·kg⁻¹, with outstanding electrochemical stability of about 97% over 10,000 charge/discharge cycles. In addition, NiCo₂S₄/g-C₃N₄ (3%) catalysts achieved 294 and 155 mV as oxygen and hydrogen evolution reaction overpotentials, respectively, at 20 and 10 mA·cm⁻² current density values. This study provides a new method for the conversion of 2D sheets and 0D colloidal network into 3D macroporous nanocomposite aerogels in multifunctional applications.

1. Introduction

Developing sustainable, environmentally friendly, and clean energy is an urgent requirement due to the growth of the population and the overutilization of fossil fuels [1, 2]. In recent days, solar cells, supercapacitors, and lithium-ion batteries are well emerged as clean energy sources [3–7]. Therefore, supercapacitor (SC) use has increased in electric vehicles, smart grid technology, and industrial power management [8, 9]. Generally, SCs have high power density, but their low energy density is the largest constraint for their

practical application. More research has been devoted to enhancing the energy density of SCs. One optimal choice is pseudocapacitive material, which is known for its high theoretical capacity [10]. Recently, nitrogen-doped carbon materials (N-doped carbon) have been increasingly used in energy storage, photocatalysis, and energy conversion applications [11, 12]. Two-dimensional (2D) graphite-like structured graphitic carbonitride (g-C₃N₄ or CN) has excellent thermal and chemical stability, a notable surface area, an attractive electronic structure, and low-cost synthesis and is environmentally friendly [11, 13–17]. Due to these excellent

properties, CN is in demand as a nanomaterial in water treatment (photocatalysis and adsorption) and energy conversion applications [12, 13, 17–21]. High nitrogen content and better electron donor properties of CN could enhance the electrochemical properties of pseudocapacitors [12, 19, 22–24].

Furthermore, ternary NiCo_2S_4 (NCS) is an SC material with rich redox active sites, a low bandgap and electronegativity, variable oxidation states, and improved electrical conductivity, ensuring fast charging and discharging of SCs [25–27]. However, the practical applications of NCS SCs have been limited due to their rapid capacitance fading and short cycling life due to the sluggish reaction kinetics and large volume changes during the charge/discharge processes. Zhang et al. reported on a tube-like NCS that achieves a specific capacitance of $1048 \text{ F}\cdot\text{g}^{-1}$ at $3.0 \text{ A}\cdot\text{g}^{-1}$ and 75.9% capacitive retention after 5,000 cycles at $10.0 \text{ A}\cdot\text{g}^{-1}$ [27]. Based on the Kirkendall effect, Pu et al. synthesized NCS hollow hexagonal nanoplates using a sacrificial template approach, providing a specific capacitance of $437 \text{ F}\cdot\text{g}^{-1}$ at $1 \text{ A}\cdot\text{g}^{-1}$ and 81% capacity retention after 1,000 cycles [26]. Poudel et al. designed zinc cobalt hydroxide/ternary sulfides on 3D carbon hollow porous carbon nanofiber, and the fabricated ASC delivered $111.72 \text{ Wh}\cdot\text{kg}^{-1}$ [28]. In addition, the composites of transition metal-based oxides or phosphides with metal-organic frameworks and polymers are emerged for supercapacitor application [29, 30]. Furthermore, Gao et al. synthesized NCS aerogel/reduced graphene oxide composite aerogels used in SCs with a specific energy of $13.4 \text{ Wh}\cdot\text{kg}^{-1}$ and oxygen evolution reaction (OER) at the overpotential 250 mV [31]. Xu et al. electrodeposited NiCo_2S_4 onto flexible graphene, showing a specific capacitance of $1348 \text{ F}\cdot\text{g}^{-1}$ at $0.5 \text{ A}\cdot\text{g}^{-1}$, and the symmetric supercapacitor device possesses $85.1 \text{ Wh}\cdot\text{kg}^{-1}$ specific energy [32]. Three-dimensional (3D) urchin-like $\text{CoNi}_x\text{S}_y/\text{CN}$ composite microspheres exhibited an ultrahigh specific capacity of $1029 \text{ C}\cdot\text{g}^{-1}$, and $\text{CoNi}_x\text{S}_y/\text{CN}/\text{activated carbon (AC)}$ provides a high specific energy of $71.9 \text{ Wh}\cdot\text{kg}^{-1}$ and capacitive retention of 72.2% after 5,000 cycles [33]. In addition, many materials were combined with CN to enhance the performance of the ASCs [20, 34–36].

However, CN is a nitrogen-doped carbon nanomaterial used in electrocatalytic reactions due to its rich nitrogen and corrosion resistance in acid and base solutions [16, 37]. Platinum- (Pt-) based electrocatalysts have been considered in electrocatalysis due to their low overpotential in alkaline conditions, but their high cost and low abundance obstruct commercialization. Another limitation is the limited OER and HER performance for the same material in the same electrolyte, hindering the inclusive efficiency of water splitting [38]. By considering the above constraints, bimetallic sulfides (specifically, NCS) have received the attention of electrochemistry researchers due to their appropriate band gap and suitable H-binding energy [39, 40]. Su et al. designed an Ru-NCS catalyst with a low OER overpotential of 190 mV at $50 \text{ mA}\cdot\text{cm}^{-2}$ and an HER overpotential of 32 mV at $10 \text{ mA}\cdot\text{cm}^{-2}$ [41]. Rebekah et al. reported on a low OER overpotential of 320 mV at $10 \text{ mA}\cdot\text{cm}^{-2}$ for an $\text{Mn}_{0.4}\text{Ni}_{0.6}\text{Co}_2\text{O}_4/\text{CN}$ electrocatalyst prepared using the hydrothermal method [42]. The nitrogen-deficient CN and

NCS composite displays a relatively low OER overpotential of 294 mV at $10 \text{ mA}\cdot\text{cm}^{-2}$ due to the synergy between the bimetallic sulfides and CN [43]. Core-shell assembly of Ni_3S_2 nanowires and CoMoP nanosheets provides 96.8 mV HER overpotential and 270 mV OER overpotential at 10 and $50 \text{ mA}\cdot\text{cm}^{-2}$ [44]. Zahra et al. reported low values of 310 and 160 mV for OER and HER, respectively, for flower-like $\text{CoNi}_2\text{S}_4/\text{CN}$ composites [45]. However, 3D aerogels/foams are predominantly advantageous for enhancing the pseudocapacitive and electrocatalytic performance by offering a high surface area and connected porous network [46, 47].

The present work reports on synthesizing a NCS/CN nanocomposite aerogel using a sol-gel colloidal self-assembly approach, considering the advantages of CN and transitional metal sulfides. The present method provides dual benefits by assembling 2D CN nanosheet-supported nanoporous NCS aerogels into multifunctional 3D macroporous aerogels. Furthermore, these composite aerogels are used in SCs and electrocatalytic oxygen and hydrogen evolution applications. The as-obtained NCS/CN composite aerogels exhibited a unique 0D/2D nanostructure and improved the electrochemical activity attributable to the NCS/CN electrode. As far as we know, no reports are available on the synthesis of NCS/CN composite aerogels using the present synthesis method and their use in electrochemical SCs and electrocatalysis.

2. Experimental

2.1. Materials. The chemicals required for the synthesis are listed in the present section. Principally, nickel nitrate hexahydrate ($\text{Ni}(\text{NO}_3)_2\cdot 6\text{H}_2\text{O}$), cobalt nitrate hexahydrate ($\text{Co}(\text{NO}_3)_2\cdot 6\text{H}_2\text{O}$), and DL-mercaptosuccinic acid (MSA) were purchased from Sigma Aldrich, Korea. Urea (Sigma Aldrich, Korea) and melamine foam were used to synthesize the CN sheets. Deionized water was used in all experiments. All precursors were used as received without further purification. Potassium hydroxide (KOH; Duksan, Korea) was used to prepare the electrolytes for electrochemical measurements. Nickel foam (MIT, Korea), PVDF (Sigma Aldrich, Korea), N-methylpyrrolidone (Duksan, Korea), carbon black (Sigma Aldrich, Korea), and AC (Duksan, Korea) were used to prepare the electrodes.

2.2. Preparation of NCS/CN Composite Aerogels. A sol-gel assembly process was used to synthesize the NCS/CN composite aerogels, followed by the conventional ethanol supercritical drying method. The $\text{Ni}(\text{NO}_3)_2\cdot 6\text{H}_2\text{O}$ (Ni precursor) and $\text{Co}(\text{NO}_3)_2\cdot 6\text{H}_2\text{O}$ (Co precursor) were dissolved in ethanol, and the concentrations for Ni^{2+} and Co^{2+} were 0.25 M and 0.5 M , respectively. In addition, 1 M MSA dissolved in ethanol was used as a sulfur source and gel accelerator. Considering a $1:2:4$ molar ratio for $\text{Ni}^{2+}:\text{Co}^{2+}:\text{S}$, an identical volume of Ni-Co nitrate and MSA solution was mixed with 5% formamide with vigorous mixing to obtain a homogeneous sol. The CN nanosheets were synthesized using the reported method [21], and detailed synthesis process is provided in supporting information (SI). The prescribed number of CN nanosheets was added to the homogeneous sol followed by ultrasonic dispersion for 15 min to consistently

mix CN nanosheets in metal sulfide sol. The above solution was stirred continuously for 2 h and kept for gelation at 60°C in an oven.

After gelation, the gel was aged in ethanol for 4 days, exchanging ethanol every 24 h. The percentage of CN sheets varied at 1%, 3%, and 5% of the Ni-Co sol, as a further increase in CN sheets constrains dispersion. Porous CN sheets were synthesized using the reported method [21]. All gels were dried using the ethanol supercritical drying method (ESCD) in a nitrogen atmosphere with ethanol supercritical conditions, and almost 6 h was required to dry all samples. The NCS aerogel was synthesized following the same process without adding CN sheets. The NCS/CN composite aerogels are denoted as CN composite aerogels, and 1CN, 3CN, and 5CN indicate 1%, 3%, and 5% CN nanosheets, respectively, in the composite with NCS.

2.3. Characterizations. The crystalline phase of the composite aerogels was obtained using an X-ray diffractometer (XRD) (Rigaku Ultima, Japan) using Cu-K α (1.54 Å) radiation in the 10° to 60° scanning range. Thermogravimetric analysis (TGA) was performed using a TA-Q500 instrument from 25°C to 1000°C with a 10°C/min heating rate in a nitrogen atmosphere. Raman spectra (LabRam Aramis, Horiba Jobin Yvon) were measured at an excitation wavelength of ~532 nm. The morphology of aerogel samples was captured using field-emission scanning electron microscopy (FESEM) (JEOL JSM-7001F). The nanosheets decorated using colloidal aerogel particles were determined by employing transmission electron microscopy (TEM) (JEOL, JEM-2100F) equipped with energy-dispersive X-ray spectroscopy (EDS) to detect the elements. X-ray photoelectron spectroscopy (XPS) (K-alpha Thermo VG, UK) was used to determine surface electronic states using a monochromatic Al X-ray source (Al-K α line: 1486.6 eV, 3 mA, and 12 kV). The surface area, pore volume, and pore size were obtained using the nitrogen adsorption/desorption method, and measurements were conducted with a surface area analyzer (Quantachrome Instruments v10.0) after degassing each sample at 150°C for 12 h.

2.4. Electrochemical Measurements. A standard three-electrode system connected to an electrochemical workstation (ZIVE instrument electrochemical workstation) was used to measure electrochemical properties. Working electrodes were prepared by drop-casting a paste comprising aerogel: carbon black: polyvinylidene fluoride diluted in NMP was 85:5:10 on Ni foam (1 × 1 cm). The aerogel mass loading of each electrode was about 2.75 mg·cm⁻². For SC applications, a 3 M KOH electrolyte using the three-electrode system (aerogel sample electrode, Pt wire as a counter, and saturated calomel electrode (SCE)) was used for electrochemical tests. The overall electrochemical performance of the prepared aerogel electrodes and ASC device was examined using cyclic voltammetry (CV), galvanostatic charge-discharge (GCD), and electrochemical impedance spectroscopy (EIS). In an ASC device, performance was measured using the two-electrode system, which combines an AC as the negative electrode and NCS/CN nanocomposite aerogel as a positive electrode. The specific energy and specific power were

both calculated by considering the total mass of the positive and negative electrodes. The OER and HER performances of the aerogel electrodes were evaluated using linear sweep voltammetry (LSV) measurements. Both OER and HER properties were measured in a 1 M KOH electrolyte with a pH of 13.7.

3. Results and Discussion

Figure 1(a) illustrates the schematic for the overall synthesis process for one-pot sol-gel assembled 3D macroporous CN nanocomposite aerogels. The presence of MSA accelerates the gelation compared to the well-established metathesis method [31]. Colloidal NCS aerogels are assembled on the 2D CN nanosheets, which further assembled 2D CN nanosheets together to form 0D@2D doubly assembled aerogels. Ultrasonication after the addition of CN nanosheets plays an important role to disperse and break the CN nanosheets into spherical form. The step-by-step schematic to obtain 3D macroporous aerogel network using 2D nanosheets is provided in Figure 1(b). The obtained CN aerogels exhibit moderate shrinkage with a bulk density of about 0.2 g·cm⁻³. The visible appearance of metal-organic sol, gel, and aerogel of NCS and CN are provided in supplementary Figure S1.

3.1. XRD, Raman Spectroscopy, TGA, and XPS. The crystalline structure of the NCS and CN composite aerogels was examined using XRD in Figure 2(a). The obtained diffraction peaks were matched with the crystalline NCS (JCPDS No. 00-011-0068), and at 23.5°, a broad hill-like peak was observed, confirming compositization with CN, and the crystalline phase of NCS was maintained [34]. Figure 2(a) shows the XRD peaks (111), (220), (311), (400), (422), (511), and (440) at 15.38°, 29.71°, 31.12°, 39.33°, 47.35°, and 55.15° 2 θ angles, respectively. No impurity peaks were found using XRD in the composite aerogels. Due to the tiny nanoparticles for NCS aerogels, XRD depicts broad diffraction peaks. The CN peaks in the XRD spectra confirm that the CN composite aerogels successfully formed. The MSA-initiated sol-gel reaction with ESCD favors the crystallization of these aerogels.

Chemical states and structural defects in the CN composite aerogels were determined using Raman spectra in Figure 2(b). The sharp Raman peaks in the 200 to 800 cm⁻¹ region and the broad hill-like peaks in the 1200 to 1700 cm⁻¹ region were observed for NCS and CN, respectively. In Raman spectra, peaks at 190, 468, and 649 cm⁻¹ confirmed the formation of crystalline NCS [48]. In addition, the graphitic nature of the CN nanosheets in the composite aerogels was determined by the presence of the D and G bands in the Raman spectra. Raman peaks of 1372 and 1550 cm⁻¹ for the D and G bands in CN were observed in these samples [49]. However, the peak intensities in the composite aerogels increased compared to those of their counterparts due to adding CN to the composite aerogels. The D/G ratios in the aerogels were determined as 1, 1.01, and 1.07, respectively, confirming that the graphitic nature of CN was maintained after the colloidal assembly using MSA in the CN composite aerogels. The Raman peaks shifted to the higher wavelength side in the CN composite

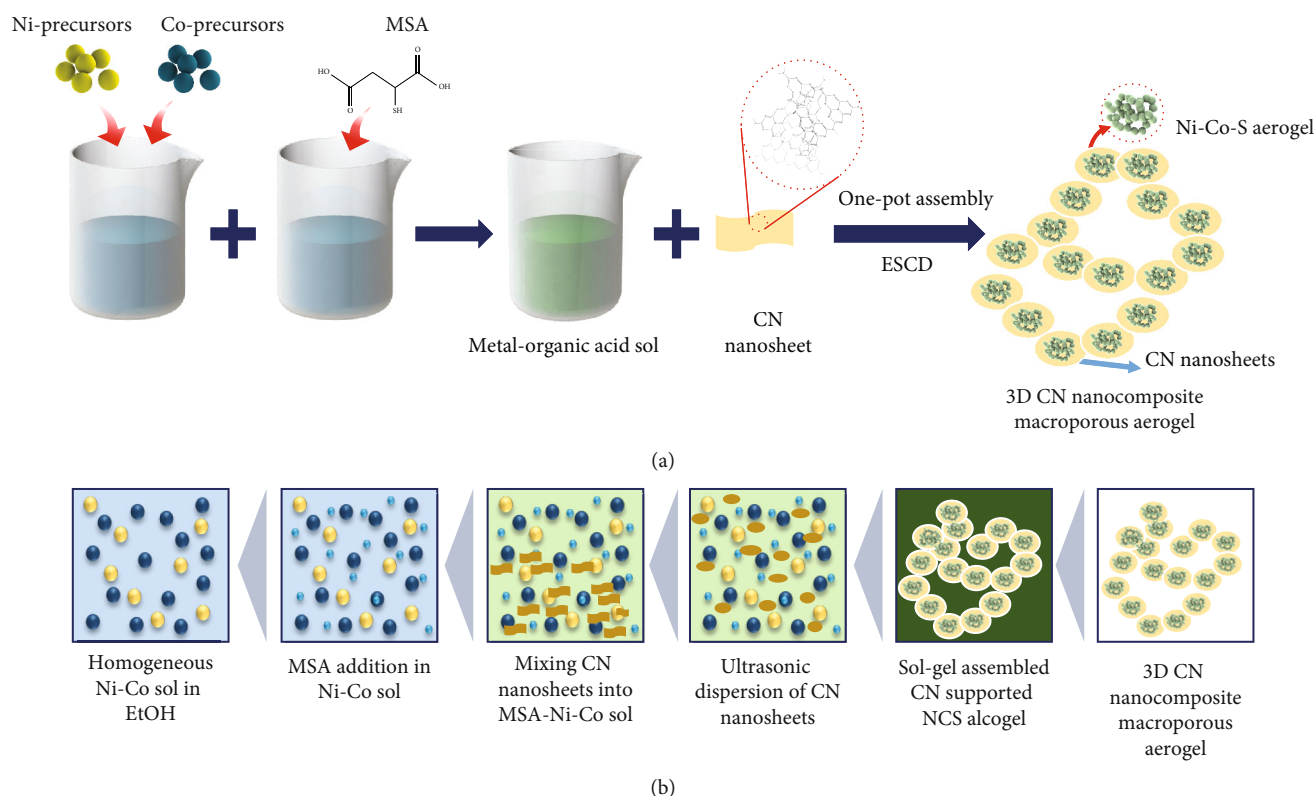


FIGURE 1: Schematic representation of the (a) in situ sol-gel-assembly process for the synthesis of 3D CN nanocomposite macroporous aerogel and (b) pathway for the formation of homogeneous metal-organic sol to 3D CN nanocomposite macroporous aerogel.

aerogels compared to the pristine NCS aerogel, confirming that the composite aerogels were successfully synthesized using this simple colloidal gel assembly approach.

The thermogravimetric analysis curves of the CN, NCS, 1CN, and 3CN aerogels are presented in Figure 2(c). The CN sample started rapid weight loss at 505°C, which was higher than the CN series aerogels (461°C and 463°C for 1CN and 3CN, respectively) and NCS aerogels (461°C). In contrast, the opposite trend for weight loss was observed, where pristine CN sheets completely decomposed after 719°C, whereas the NCS, 1CN, and 3CN composite aerogels displayed weight loss percentages of 31.18%, 33.18%, and 43.19%, respectively, after 1,000°C. This weight loss was due to the decomposition of CN in composite aerogels. The CN in composite aerogels was estimated as 2.64% and 10% for 1CN and 3CN, respectively.

The XPS technique was further used to investigate the chemical state and elemental composition of NCS/CN (3CN) colloidal-assembled composite aerogels. The XPS survey scan spectra for CN, NCS, and 3CN composite aerogels presented in Figure 2(d) confirm the presence of Ni, Co, S, C, N, and O elements in the composite aerogels. Figure 2(e) displays the high-resolution spectra for C 1s, further divided into two prominent peaks at 284.8 and 288.1 eV, attributing to the C=C/C-C and C=N of CN, respectively [50]. An additional peak observed at 285.34 eV can be assigned to C-O/C-S, confirming the strong bonding between the NCS and CN sheets. For high-resolution N 1s spectra (Figure 2(f)), three characteristic peaks were

obtained at 398.7, 399.6, and 400.9 eV, corresponding to the pyridinic, pyrrolic, and graphitic nitrogen present in the CN. The presence of pyridinic N can activate more CN aerogel surface, where the N atoms provide electrons delocalized on the entire surface, resulting in improving charge transfer by facilitating the surface reduction reaction beneficial for electrochemical energy storage and HER/OER process. The N-containing surface functional groups can improve the wettability of the electrode and its pseudocapacitive nature. The 3CN sample shows notable specific capacitance value; further increase in CN amount decreases the specific capacitance. It was due to the decrease in specific surface area that resulted in reducing electrode-electrolyte interface [51]. The Ni 2p spectrum (Figure 2(g)) is further deconvoluted into two primary peaks: spin-orbit states at 873.7 eV (Ni 2p_{1/2}) and 855.9 eV (Ni 2p_{3/2}), and two satellite peaks at 880.2 eV and 861.6 eV, respectively. The Ni 2p_{3/2} and Ni 2p_{1/2} peaks were fit at 852.5 and 855.9 eV and at 870.1 and 873.7 eV binding energy positions, corresponding to Ni²⁺ and Ni³⁺, respectively [25]. The higher valence states of Ni (oxidized Ni (Ni²⁺, Ni³⁺) and satellite) were due to the partial oxidation of Ni on the aerogel catalysts surface in air exposure, while lower valence state was attributed to metallic Ni. Similarly, Co 2p spectra can be deconvoluted into metallic Co and oxidized Co, leading to the transfer of electrons from electrons from Co to Ni [52]. Figure 2(h) presents high-resolution Co 2p spectra, deconvoluted at 781.2 and 797.3 eV and attributed to Co 2p_{3/2} and Co 2p_{1/2}, respectively. These peaks were further fit, respectively, at 778.1

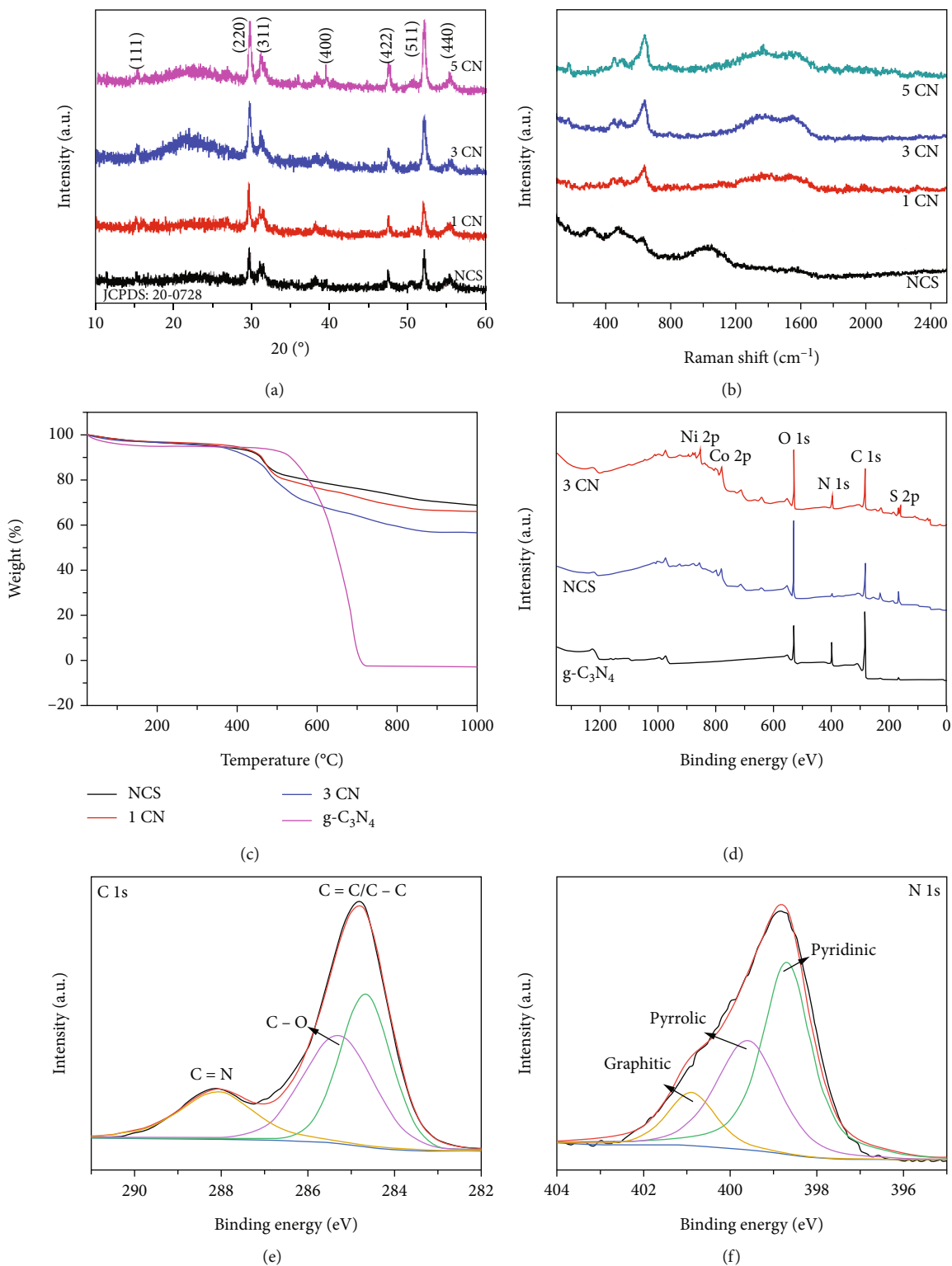


FIGURE 2: Continued.

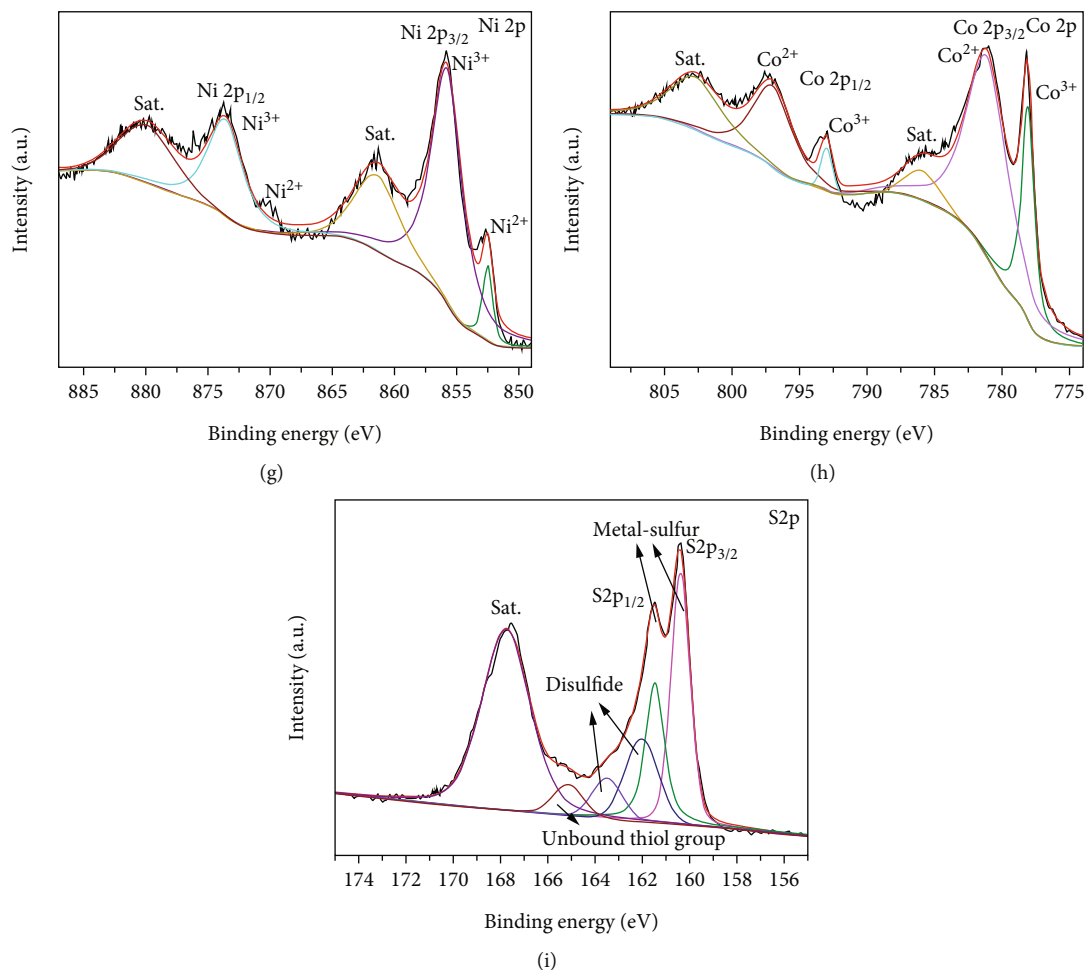


FIGURE 2: (a) XRD and (b) Raman spectra for NCS aerogel and NCS/CN composite aerogels (1CN, 3CN, and 5CN). (c) TGA profiles for g-C₃N₄, NCS aerogel, and NCS/CN composite aerogels (1CN and 3CN). (d) XPS survey scan spectrum for g-C₃N₄, NCS aerogel, and 3CN composite aerogels. (e–i) High-resolution XPS spectra for C 1s, N 1s, Ni 2p, Co 2p, and S 2p regions of 3CN composite aerogels.

and 793 eV attributed to Co³⁺ and 781.3 and 797.2 eV for Co²⁺ [25]. The S 2p spectrum (Figure 2(i)) consists of two prominent peaks at binding energy positions of 161.4 and 162.4 eV, corresponding to S 2p_{1/2} and S 2p_{3/2}, respectively [53]. The additional peak at 168.5 eV was attributed to the higher oxidation state of S₂O₃⁻ due to the partial oxidation of NCS in the air. The high-resolution S 2p XPS suggest the existence of metal-sulfur, disulfide, and unbound thiol groups as presented in Figure 2(i). The high-resolution XPS peaks for pristine g-C₃N₄ nanosheets and NCS aerogels are provided in Figure S2 (SI). The comparison between the XPS spectra for C 1s and N 1s peaks in pristine g-C₃N₄ and same in CN nanocomposite aerogels clearly confirms the shift in binding energy. In addition, the binding energy shift was observed in Ni 2p, Co 2p, and S 2p peaks, respectively, for CN nanocomposite aerogels compared to the NCS aerogel. The overall XPS study proves the assembly of 3D nanocomposite aerogel using facile in situ sol-gel assembly process.

3.2. Morphological and Porosity Features. The morphology of CN nanocomposite aerogels is presented in Figure 3.

The SEM images for the pristine NCS aerogels and CN nanosheets are provided in Figures 3(a) and 3(e). Figures 3(b)–3(d) present SEM images for CN nanocomposite aerogels (1CN, 3CN, and 5CN). The microstructure of the NCS aerogels comprises connected nanoparticle clusters forming a porous network, confirming the formation of an aerogel network using the MSA-assisted colloidal assembly method. The nanocluster size of the NCS aerogel is around 30 to 50 nm. The CN nanosheets were observed in Figure 3(e). The addition of the CN (3CN aerogel; Figure 3(c)) creates a sandwich-like structure, where the colloidal NCS nanoparticles are assembled on the CN nanosheets. This sandwich-like morphology provides a more synergistic effect to enhance the electrochemical properties of the composite aerogels. Furthermore, the higher amount of CN (5CN aerogel in Figure 3(d)) demonstrates a more complex and agglomerated network and degrades the properties of the aerogels.

Furthermore, transmission electron microscopy was analyzed to provide better information about the nanointeractions between NCS and CN in composite aerogels. The synthesis method used for CN nanosheets provides pores as seen in Figure S3. Figures 4(a) and 4(b) depict 0D

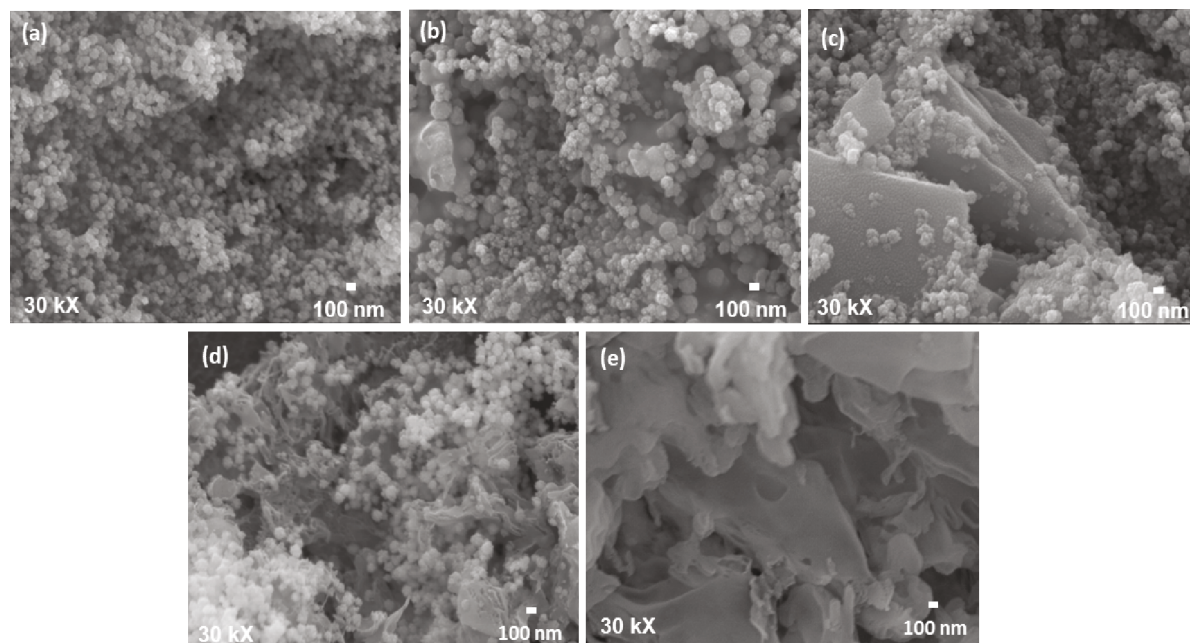


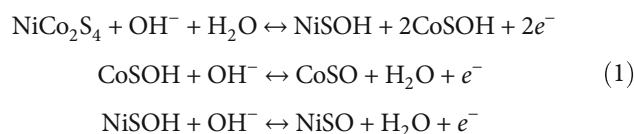
FIGURE 3: SEM images for (a) NCS aerogel, (b–d) NCS/CN composite aerogels (1CN, 3CN, and 5CN), and (e) CN nanosheets.

nanoparticles anchored on the CN nanosheets, and CN nanosheets assembled to form 0D@2D composite aerogels. However, the pristine NCS aerogels display a highly porous necklace-like network with a uniform arrangement of 10 to 20 nm nanoparticles (SI Figure S4). Thus, the MSA-assisted colloidal sol-gel assembly provides a finely structured nanonetwork of 0D@2D CN composite aerogels. The lattice fringes in Figures 4(c)–4(e) for CN aerogels prove that the NCS aerogels are crystalline, and this lattice fringe was 0.55 nm, corresponding to the (111) planes of NCS [54]. A dot-ring diffraction pattern was observed in selected area electron diffraction (Figure 4(f)), confirming that these nanocomposite aerogels are polycrystalline, similar to the XRD results (Figure 2(a)). From the overall TEM study, it is clearly observed that 2D CN nanosheets are assembled together by conversion of its rectangular nanosheet structure (Figures S3 and S5) to the spherical nanosheets supported by NCS aerogel network (Figure 4(a)). It was due to the presence of MSA and metal nanoparticles (Ni^{2+} , and Co^{2+}) in NCS, supported by the network of metal alloy-based aerogels [55, 56]. In addition, EDS mapping for the composite aerogel was performed to confirm the structure further (Figures 4(g)–4(l)) and confirm all elements in the CN composite aerogels are uniformly distributed in the network, which better interacts with electrolytes during electrochemical measurements. The elemental ratio for 3CN nanocomposite aerogel is provided in table S1 (SI).

The N_2 adsorption/desorption isotherms and pore-volume profiles for the NCS/CN composite aerogels are provided in Figures 5(a) and 5(b). Composite aerogels and their counterpart pristine NCS aerogel and CN nanosheets display type III isotherms with H3 hysteresis loops [31]. The calculated surface area values using the Brunauer–Emmett–Teller method are 26.91, 72.92, 66.57, 81.77, and 64.82 $\text{m}^2\cdot\text{g}^{-1}$ for CN, NCS aerogel, 1CN, 3CN, and 5CN composite aerogels,

respectively (SI table S2). The CN was prepared by burning urea at 500°C; hence, its surface area value is lower than that of the aerogels. However, the 3CN composite aerogel has a higher surface area than other composites due to the well-arranged assembly of NCS and CN and sandwich-like microstructure confirmed using SEM (Figure 3). In comparison with the reported sulfide-based aerogels, the MSA-assembled NCS/CN composite aerogels have a higher specific surface area. Pore size and pore volume values are calculated using the BJH method in Figure 5(b). For all aerogel samples, mesopores between 10 and 15 nm were observed. The surface area, pore volume, and pore size values for the NCS/CN composite aerogels and their counterparts were improved compared with the reported values for bulk CN composite materials.

3.3. Electrochemical Performance of NCS/CN Nanocomposite Aerogels. Self-assembled CN nanocomposite aerogels were used to examine their electrochemical SC properties. Figure 6(a) compares the CV spectra for NCS and CN composite aerogels (1CN, 3CN, and 5CN) at a 5 $\text{mV}\cdot\text{s}^{-1}$ scan rate. The comparison for the GCD profiles at a 10 $\text{mA}\cdot\text{cm}^{-2}$ current density is provided in Figure 6(b). All CV curves include a pair of redox peaks due to the reversible transitions of $\text{Ni}^{2+}/\text{Ni}^{3+}$ and $\text{Co}^{2+}/\text{Co}^{3+}/\text{Co}^{4+}$ associated with OH^- and the possible pseudocapacitive reaction mechanism is provided in the following equations [25, 57].



The area under the curve for the 3CN aerogels is more prominent than other composite aerogels (1CN and 5CN)

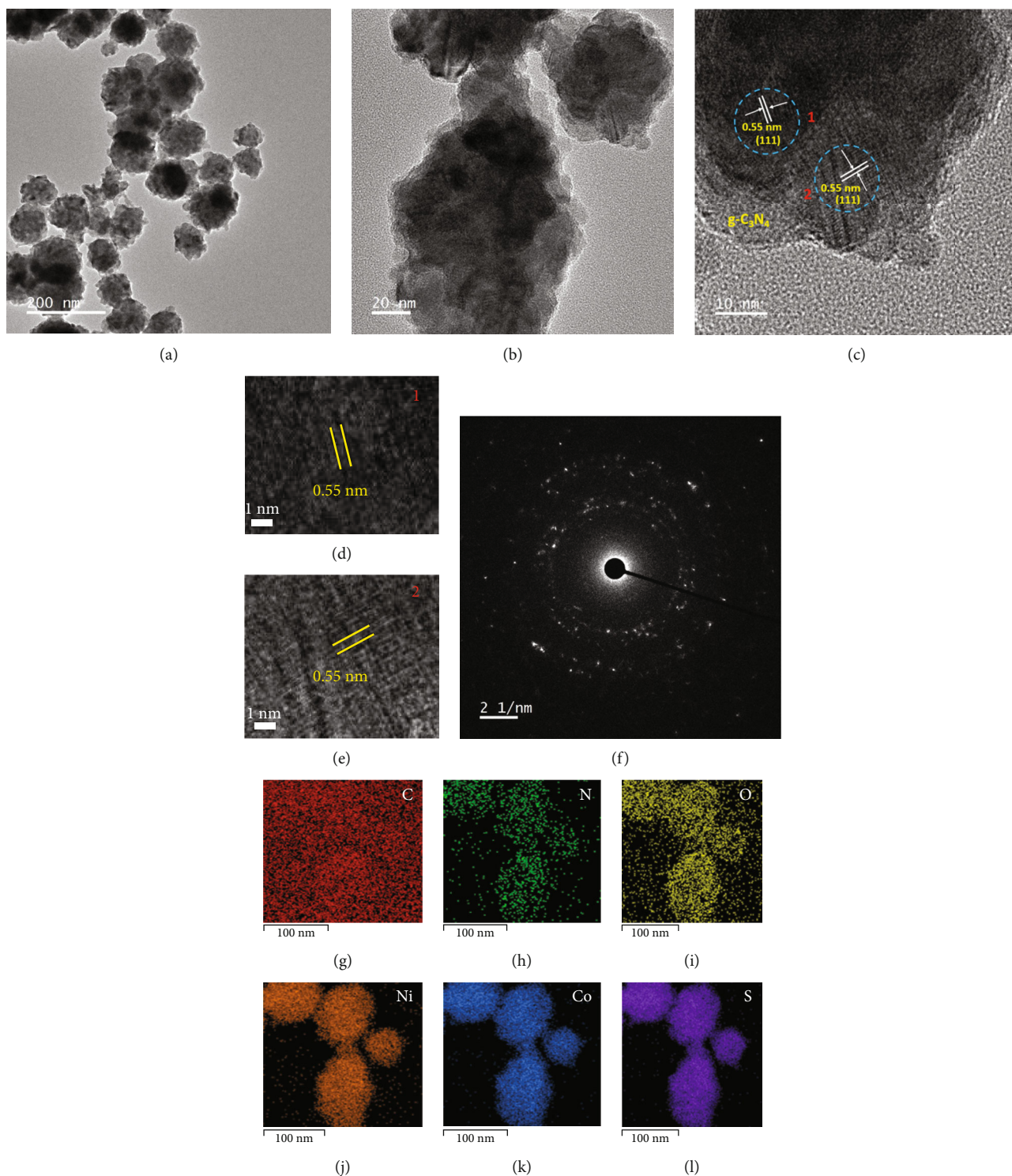


FIGURE 4: (a) TEM images and (b–e) high-resolution TEM images for NCS/CN composite aerogel (3CN), (f) SAED pattern, and (g–l) EDS mapping for NCS/CN composite aerogel (3CN).

and NCS aerogels alone. Similar behavior was observed in GCD curves in Figure 6(b), following the order of $5\text{CN} > \text{NCS} > 1\text{CN} > 3\text{CN}$, indicating improved charge storage capacity for 3CN nanocomposite aerogels after self-assembling 3% CN nanosheets with NCS aerogels. This outcome confirms that CN nanosheets can adsorb electro-

lyte ions on the composite aerogel electrode surface. In addition, Ni foam substrate was used as a current collector, demonstrating a negligible CV area compared to the aerogel samples, confirming that Ni foam cannot contribute to the specific capacitance of the composite aerogels. The CV curves for 3CN composite aerogel electrodes at 5 to

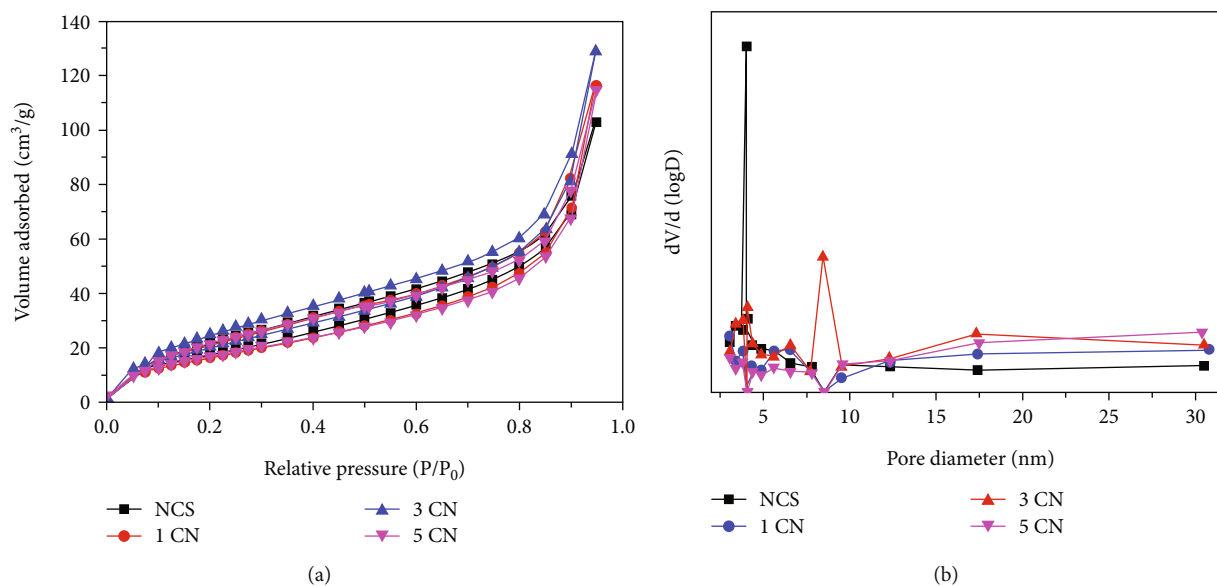


FIGURE 5: (a) N_2 adsorption-desorption and (b) pore-size distribution for NCS aerogel and NCS/CN composite aerogels.

100 $mV \cdot s^{-1}$ scan rates are provided in Figure 6(c), and CV profiles for the NCS, 1CN, and 5CN samples are provided in Figure S6 (SI) to investigate the electrochemical properties of the overpotential window of 0 to 0.5 V/SCE in an alkaline electrolyte. The gradual increase in the peak current for the scan rate and the symmetric nature of all CV curves confirm the reversible redox reactions. Anodic and cathodic oxidation peaks for all CV profiles moved toward higher and lower potential values, respectively.

Furthermore, Figure 6(d) depicts the symmetric behavior of cathodic and anodic peak currents at various scan rates. The electrode charge storage properties were determined using the power law relation, where $b = 0.48$ is the slope of the $\log(\text{peak current})$ versus $\log(\text{scan rate})$ graph (Figure S7 (SI)). This result confirms that the composite aerogel electrodes exhibit improved charge storage due to diffusion-controlled charge storage rather than the capacitive charge storage mechanism [58].

Furthermore, the diffusive (bulk charges) and capacitive (surface charges) contributions of the specific current density were evaluated using the modified power law [3]. Figure 6(e) depicts the current contribution calculated using CV profiles for 3CN nanocomposite aerogels, and that for other aerogel electrodes (NCS, 1CN, and 5CN) is provided in Figure S8 (SI). The figures reveal that the surface charge (pseudocapacitive) contribution increases with the scan rate for all samples and that, for the battery type (bulk), it is decreased with the scan rate. The pseudocapacitive charge contribution is higher for NCS aerogel electrodes; however, the CN nanocomposite aerogels have higher battery-type charges. The GCD curves for the 3CN composite aerogels are presented in Figure 6(f), and those for NCS, 1CN, and 5CN, aerogel electrodes are provided in supplementary Figure S6 with a potential window from 0 to 0.45 V/SCE at 10 to 30 $mA \cdot cm^{-2}$ current density values. All electrodes display relatively similar GCD profiles;

specifically, the 3CN nanocomposite aerogel electrode has a longer charge-discharge time, indicating more energy storage capacity.

Figure 6(g) provides calculated specific capacitances using GCD profiles and equations (S1) for all aerogel electrodes. The 3CN composite aerogel electrode achieved 1083, 992, 875, 785, and 730 $F \cdot g^{-1}$ at 10, 15, 20, 25, and 30 $mA \cdot cm^{-2}$ current density values, respectively, for the SCs. This decrease in specific capacitance values with the increase in current density values was due to the fast diffusion rates for electrolyte ions [59]. The 67.4% approximate reduction in the specific capacitance values at 30 $mA \cdot cm^{-2}$ confirms better electrode rate performance for the 3CN composite aerogel. The specific capacity values for all aerogel electrodes are presented in table S3 (SI), and the 3CN nanocomposite aerogel possesses specific capacities from 328.90 to 487.34 $C \cdot g^{-1}$. Figure 6(h) displays the Nyquist plots for NCS, 1CN, 3CN, and 5CN nanocomposite aerogels over 1 MHz to 1 kHz, with the corresponding equivalent circuit in the inset of the figure. The 3CN composite aerogel electrode achieved $R_s = 0.63 \Omega \cdot cm^{-2}$, much lower than the NCS aerogels alone ($0.85 \Omega \cdot cm^{-2}$). In addition, the EIS-fitted circuit (Figure S9 (SI)) and R_s and R_{ct} values for all NCS and CN nanocomposite aerogels are tabulated in table S4 (SI).

The electrochemical stability for NCS and 3CN nanocomposite aerogel electrodes was measured for 10,000 GCD cycles at 50 $mA \cdot cm^{-2}$ (Figure 6(i)). A gradual decrease in electrochemical capacitance was found for the NCS aerogels; however, the 3CN composite aerogel electrode is more stable. The first and last 6 consecutive GCD cycles for 3CN aerogel are provided in the inset of Figure 6(i) to determine the stability of 3CN aerogels. The electrochemical capacitive retention for the NCS and 3CN aerogel electrodes was 62% and 87.03% over 10,000 GCD cycles, respectively, confirming that the assembly of CN nanosheets over NCS

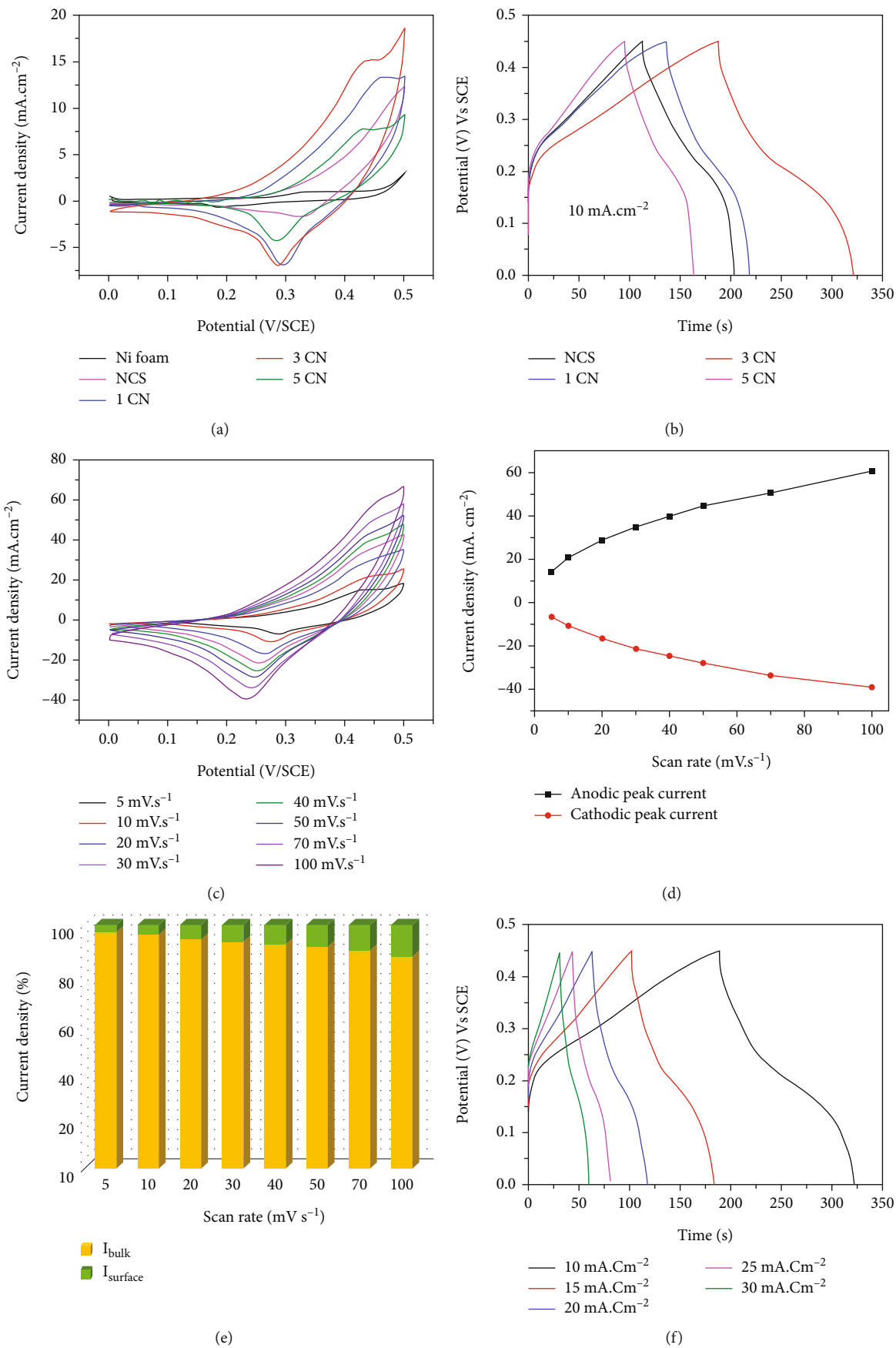


FIGURE 6: Continued.

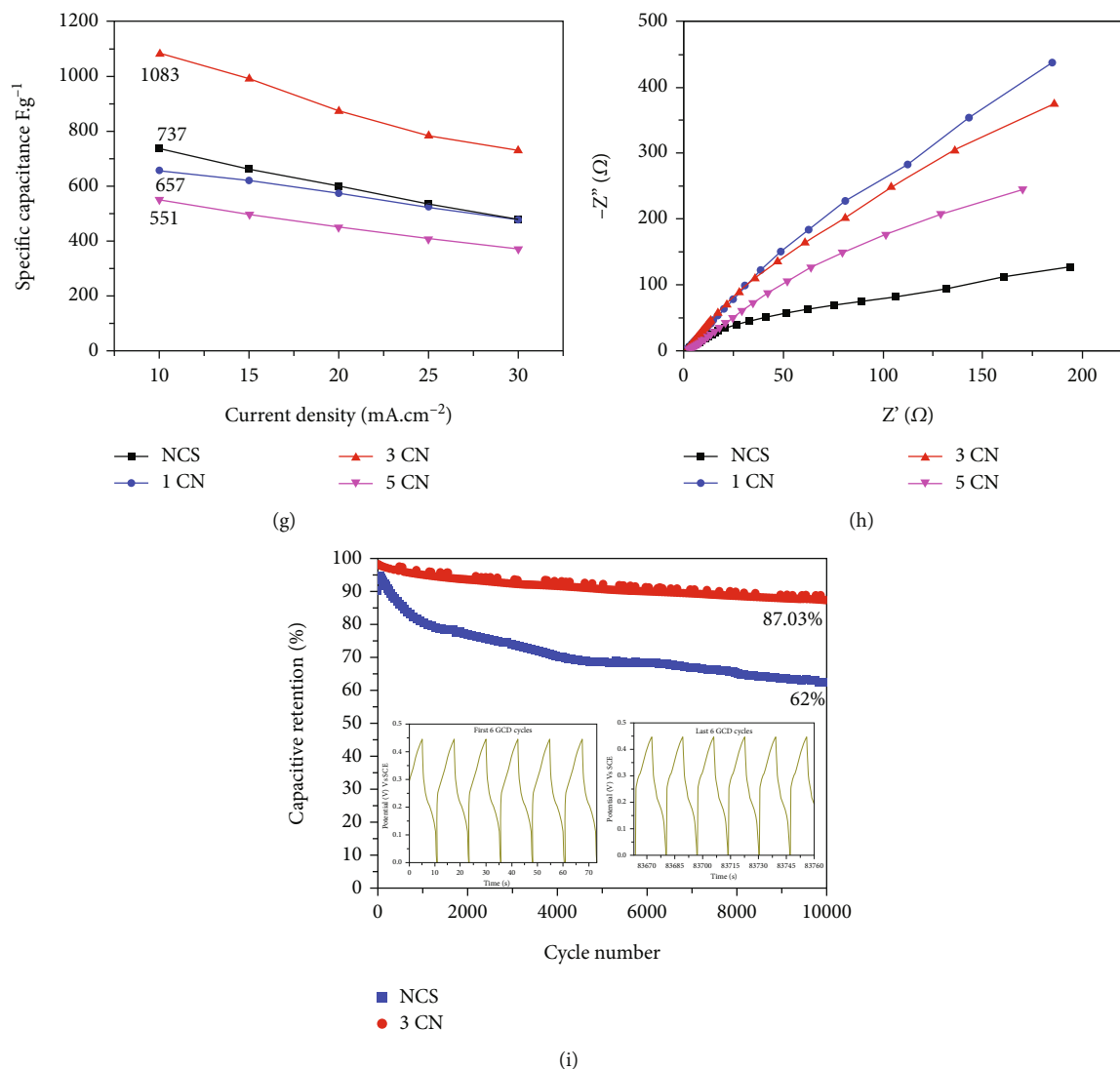


FIGURE 6: (a, b) Comparison of the CV and GCD profiles for NCS aerogel and NCS/CN composite aerogels (1CN, 3CN, and 5CN) at a scan rate of $5 \text{ mV}\cdot\text{s}^{-1}$, and a current density $10 \text{ mA}\cdot\text{cm}^{-2}$. (c) CV curves of 3CN composite aerogels at various scan rates. (d) Cathodic and anodic peak current values at different scan rates. (e, f) GCD curves of 3CN composite aerogels at different current densities. (g) Specific capacitances and (h) EIS spectra of NCS aerogel and NCS/CN aerogels (1CN, 3CN, and 5CN) and (i) cyclic stability of NCS aerogel and 3CN composite aerogels (inset shows first and last 6 GCD cycles).

nanospheres improves stability by 25%. The in situ sol-gel colloidal assembly approach between CN nanosheets and NCS nanospheres to produce nanosandwiches supported by Ni foam provides a more porous network, good contact, and increased average faradic capacitance values. A comparison of electrochemical properties for NCS-based aerogel electrodes with the sol-gel-assembled CN nanocomposite aerogels is provided in supplementary table S5. The proposed aerogels display remarkable electrochemical properties (specific capacitance and cyclic stability) over the reported NCS-based aerogel electrodes.

3.4. Electrochemical Performance of NCS/CN Composite Aerogels//AC Asymmetric Supercapacitor. A prototype 3CN aerogel//AC ASC was fabricated using 3CN aerogel as a positive electrode and AC as a negative electrode, respectively,

and a separator was used between the two electrodes. A 3 M KOH electrolyte was used to measure the electrochemical performance of the device using the two-electrode system. The proposed design for the ASC device is presented in Figure 7(a). Furthermore, mass loading for the negative electrode (AC) was adjusted to construct the ASC using Eq. S4 to balance the electrode charges.

The CV curves of 3CN aerogel and AC electrodes at a $10 \text{ mV}\cdot\text{s}^{-1}$ scan rate at -1 to 0 V and 0 to 0.5 V are provided in Figure 7(b). The operational potential window for ASC was optimized using the CV curves of the ASC at various potential windows, and for the 3CN//AC ASC device, the extended window could be 1.5 V (Figure 7(c)), which is comparable with the reported NCS-based ASC. In addition, CV curves at various scan rates with a constant potential window of 1.5 V are provided in Figure 7(d). The symmetric

behavior for all CV curves confirms the ideal capacitive behavior. Figure S10 (SI) shows the GCD curves for HSC at different potential windows. In addition, the GCD curves for ASC at 2 to 20 mA current are presented in Figure 7(e), confirming the triangular nature. Overall, the CV and GCD curves for the 3CN aerogel//AC ASC device highlight the electrochemical competencies at various potential windows and currents, respectively.

Furthermore, Figure 7(f) provides the specific capacitances of the ASC device calculated from Eq. S5 and the I curves in Figure 7(e). The calculated values of specific capacitance for the ASC device were 137, 122, 115, 110, 109, 107, 97, and 92 F.g⁻¹ at 2, 4, 6, 8, 10, 12, 16, and 20 mA, respectively, which is the usual behavior for a capacitance decrease with increased current values. Figure 7(g) presents the Ragone plot for comparison of specific energy and specific power calculated using Eqs. S6 and S7 (SI), with the reported values. The 3CN//AC ASC achieved a maximum energy density of 43 Wh.kg⁻¹ and a minimum power density of 88.23 W.kg⁻¹ compared to the other reported ASCs [25, 60–66]. In addition to this, the comparison of electrochemical performances for reported aerogel and CN-based devices is tabulated in table S6 (SI).

For practical applications of SC devices, long-term stability has more importance. Hence, we measured the cyclic stability of the 3CN aerogel//AC ASC device using the GCD measurement at 50 mA, as presented in Figure 7(h). The ASC device has 97% cyclic stability at a 50 mA current over 10,000 cycles. The increased stability for the ASC device compared to the 3CN electrode was due to the combination of CN and AC, making the ASC device more stable. The electrochemical impedance spectroscopy spectra for the prototype ASC device before and after stability are presented in Figure 7(i), demonstrating the same approximate R_s value. In conclusion, the fabricated 3CN aerogel//AC ASC device has a great advantage for practical applications due to its long-term stability and remarkable energy density at a low power density.

3.5. Electrocatalytic Oxygen and Hydrogen Evolution Reaction. The electrocatalytic activity of CN aerogels depends on the intrinsic activities and density of electroactive sites. The density of electroactive materials can be determined by evaluating the electrochemical active surface area (ECSA) related to the electrochemical double-layer capacitance (C_{dl}) of the materials [67]. The CVs for all samples were measured in the small potential range with no any redox peak in the range of potential 0–0.2 V/SCE as presented in Figure S11 (a–d) of SI. The capacitance currents at the open circuit potential of each CV in Figure S11 (a–d) for different scan rates were used to calculate C_{dl} values using Eq. S8. The C_{dl} values for CN nanocomposite aerogels are 0.98, 0.87, 2.20, and 0.47 mF.cm⁻² for NCS, 1CN, 3CN, and 5CN aerogel composites, respectively. Eq. S9 in SI was used to determine ECSA values, and CN nanocomposite aerogels possess 24.4, 21.7, 54.5, and 11.8 cm² for NCS, 1CN, 3CN, and 5CN aerogels, respectively. The 3CN aerogel catalyst demonstrates very high C_{dl} and ECSA values than the other presented catalysts consistent with BET surface area values. These observations reveal that

the electrochemical catalytic activity of NCS/CN composite aerogels was due to the exposure of all active sites and uniform distribution of NCS colloidal aerogels onto 2D CN nanosheets of this nanosandwich-like aerogels.

The electrocatalytic OER and HER activities of the prepared composite aerogel catalysts were evaluated using LSV in the presence of a 1 M KOH electrolyte. The synergistic effect of C- and N-rich species and Co³⁺ metal ions in composite aerogels develops rich adsorption sites for adsorbing intermediates formed during the oxidation of water molecules. In addition, the suppressed aggregation of CN nanosheets using assembled metal cations in NCS produces more adsorbing intermediates, which are further responsible for OER. Furthermore, OER LSV profiles for the developed aerogel catalyst are presented in Figure 8(a) in the range of 1.1 to 2 V vs. RHE at a constant scan rate of 5 mV.s⁻¹. The OER overpotential was converted from SCE to RHE using Eq. S10. At a 20 mA.cm⁻² current density, the overpotential values were 323, 301, 294, and 363 mV for the pristine NCS, 1CN, 3CN, and 5CN composite aerogel catalysts, respectively (Figure 8(b)). The 3CN composite aerogel catalyst reveals a low OER overpotential of 294 mV compared to the others. The metal ions in Ni and Co in NCS were well intercalated with the CN nanosheets for the 3CN composite aerogels, confirming the morphology and other properties.

Additionally, the redox pair formation on the Ni and Co intermediates resulted in the transfer of charges and formation of Co⁴⁺ cations, leading to enhanced electrophilicity due to the intermediate product O-OH [68]. However, the inductive effect predominates, and the fast withdrawal of electrons by subsequent adsorption of intermediates resulted in a remarkably low overpotential for the 3CN aerogel electrocatalyst. The high OER overpotential for other aerogel composites was due to the poor kinetics in absorbing intermediate products formed during transfer for the oxidation states by the Ni and Co species [69]. However, OER kinetics were studied using the fitted Tafel plots in Figure 8(c), and 3CN catalysts have a 126 mV.dec⁻¹ Tafel value, which is lower than the other composite aerogel catalysts, such as NCS, 1CN, and 5CN, with corresponding Tafel slopes of 174, 147, and 317 mV.dec⁻¹, respectively.

The HER catalytic activity for the prepared CN nanocomposite aerogel catalysts was investigated in conditions similar to those in OER. Figure 8(d) presents the HER LSV curves of the NCS, 1CN, 3CN, and 5CN composite aerogel catalysts. The HER overpotential was converted from SCE to RHE using Eq. S10 at 10 mA.cm⁻². The 3CN catalyst displayed a low HER overpotential of 155 mV vs. RHE compared to the other catalysts of NCS, 1CN, and 5CN as 180, 203, and 195 mV, respectively, at a 10 mA.cm⁻² current density (Figure 8(e)). Furthermore, the Tafel plots for composite aerogel catalysts are provided in Figure 8(f). The 3CN catalyst has a low Tafel slope of 81 mV.dec⁻¹, which is satisfactorily lower than the other NCS, 1CN, and 5CN catalysts with Tafel slope values of 101, 131, and 100 mV.dec⁻¹, respectively. Furthermore, Figure 8(g) reveals that the 3CN composite aerogel catalysts demonstrate remarkable OER potentiometric stability over 24 h with a constant potential of 1.57 V at a 100 mA.cm⁻² current density. In addition to

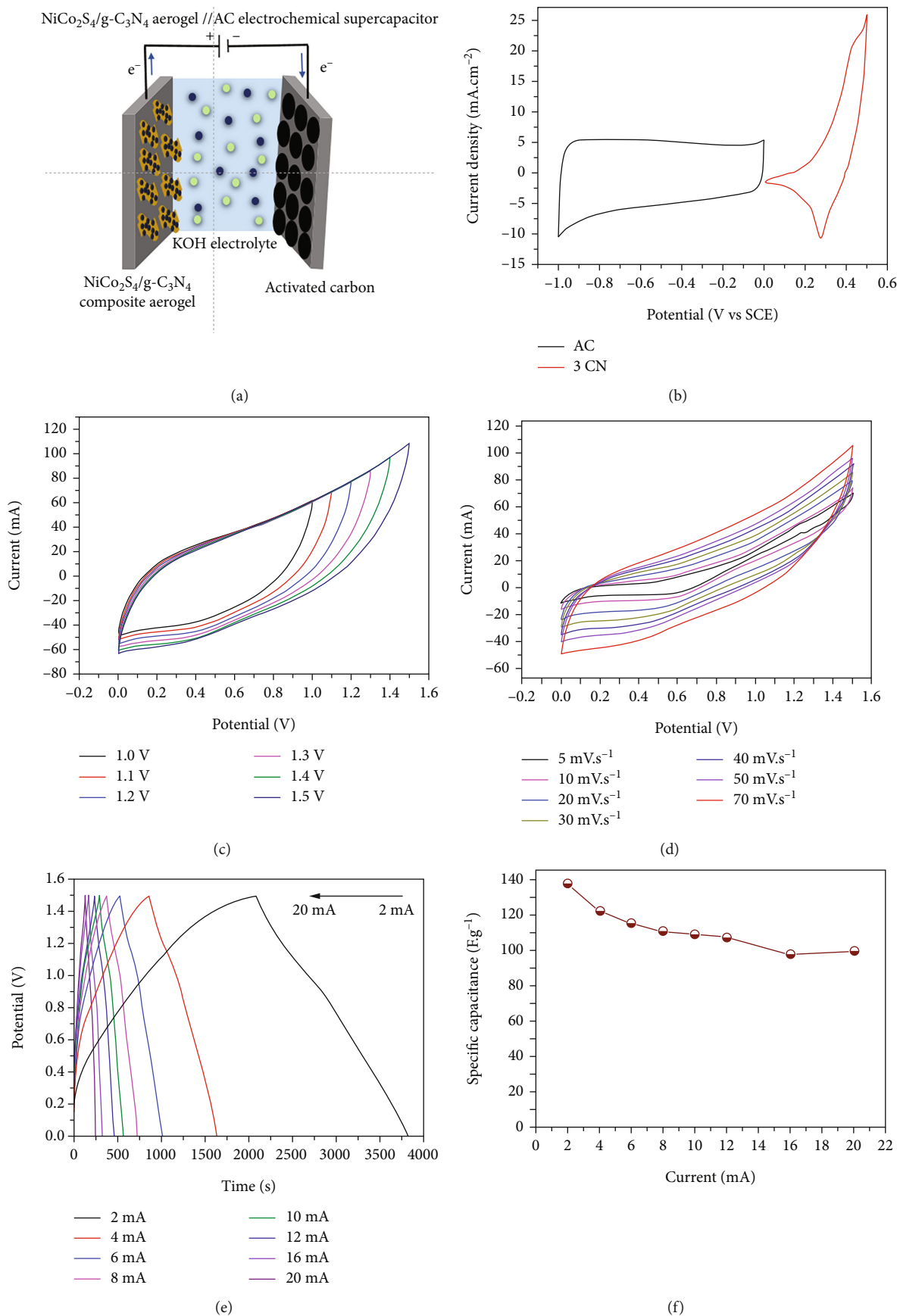


FIGURE 7: Continued.

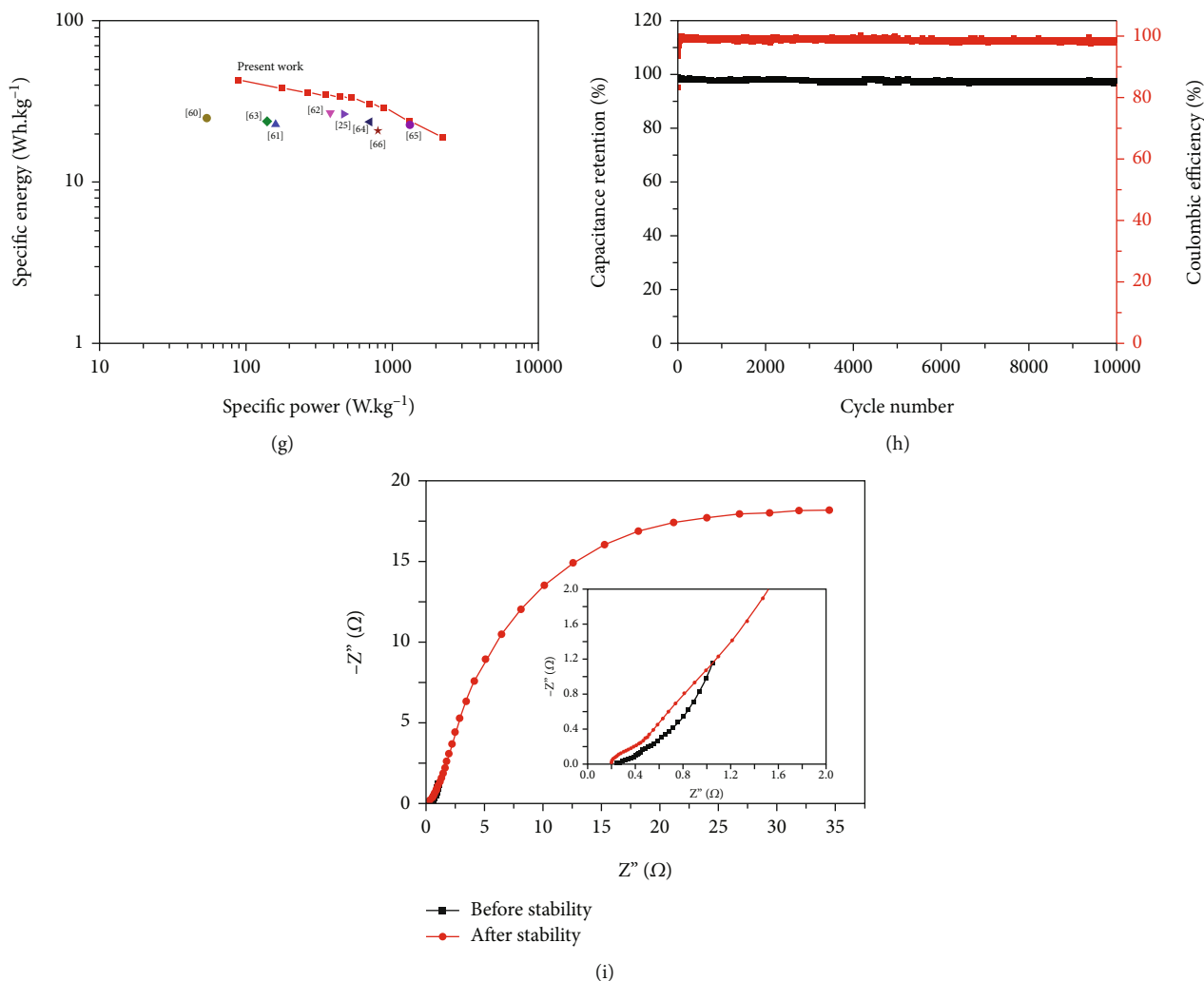


FIGURE 7: (a) Schematic illustration of an assembled NCS/CN composite aerogel//AC ASC device. (b) CV curves of 3CN and AC at a scan rate of $10 \text{ mV}\cdot\text{s}^{-1}$, (c) CV curves at different potential windows, and (d) at different scan rates of NCS/CN composite aerogel//AC ASC. (e) GCD profiles and (f) specific capacitances of NCS/CN composite aerogel//AC ASC. (g) Ragone plot of specific energy and the specific power of NCS/CN composite aerogel//AC ASC compared with reported values. (h) Cyclic stability at 50 mA and (i) EIS spectra for NCS/CN composite aerogel//AC ASC.

this, HER potentiometric stability presented in Figure S12 (SI) confirms the stability of 3CN aerogel catalyst at $100 \text{ mA}\cdot\text{cm}^{-2}$ current density. It was further supported by OER and HER polarization curves presented in Figure S13 (SI) after 24 h stability test, which shows $\sim 10 \text{ mV}$ difference in both OER and HER overpotential compared to the same values reported before 24 h stability test. Furthermore, the XRD, EDAX, FESEM, and TEM results after 24 h OER and HER stability tests are provided in Figure S14 and S15 (SI), confirming the 3D aerogel structure intact. Comparing the results for the proposed catalyst with the reported catalysts is essential to explain how the proposed catalyst is advantageous compared with the other reported catalysts.

The comparison for OER and HER overpotentials with reported electrocatalysts was provided in Figures 8(h) and 8(i). The OER overpotential for the presently reported 3CN nanocomposite aerogel electrocatalyst is 294 mV at a $20 \text{ mA}\cdot\text{cm}^{-2}$ current density. However, other electrocatalysts,

such as Fe- Co_9S_8 @CoO (296 mV) [70], Au@ NCS (299 mV) [71], COF/graphene (300 mV) [72], Ni_3Fe /reduced graphene oxide (308 mV) [73], CoNi_2S_4 [74], CO_3S_4 - MoS_2 [75], Ni@Ru/CNS [76], Ir-Ni (365 mV) [77], and NiFe_2O_4 (380 mV) [78], have higher overpotential values at a $10 \text{ mA}\cdot\text{cm}^{-2}$ current density. In addition, the present 3CN electrocatalyst has an HER overpotential value of about 155 mV at $10 \text{ mA}\cdot\text{cm}^{-2}$. The corresponding HER overpotential value is better than the following reported electrocatalysts: CN/ Fe_3O_4 / MoS_2 [79], CoS_2 /graphene [80], MoS_2 /S-doped CN [81], MoS_2 /PANI [82], Ni/NCA [83], Pd-NCS [84], CoP@C-NPs/GA-5 (225 mV) [85], Ni: Co_3S_4 (199 mV) [86], and MoS_2 aerogel [87].

The several other unique catalysts, such as Ni_2P -MnP@ Co_2P [88], nickel molybdenum phosphide (Ni-Mo-P) [67], cobalt molybdenum phosphide (Co-Mo-P) [67], and cobalt nickel phosphide (Co-Ni-P) [67], in the single ultrathin-3D-nanosheets on nickel foam, FeS_2 - MoS_2 @ CoS_2 -

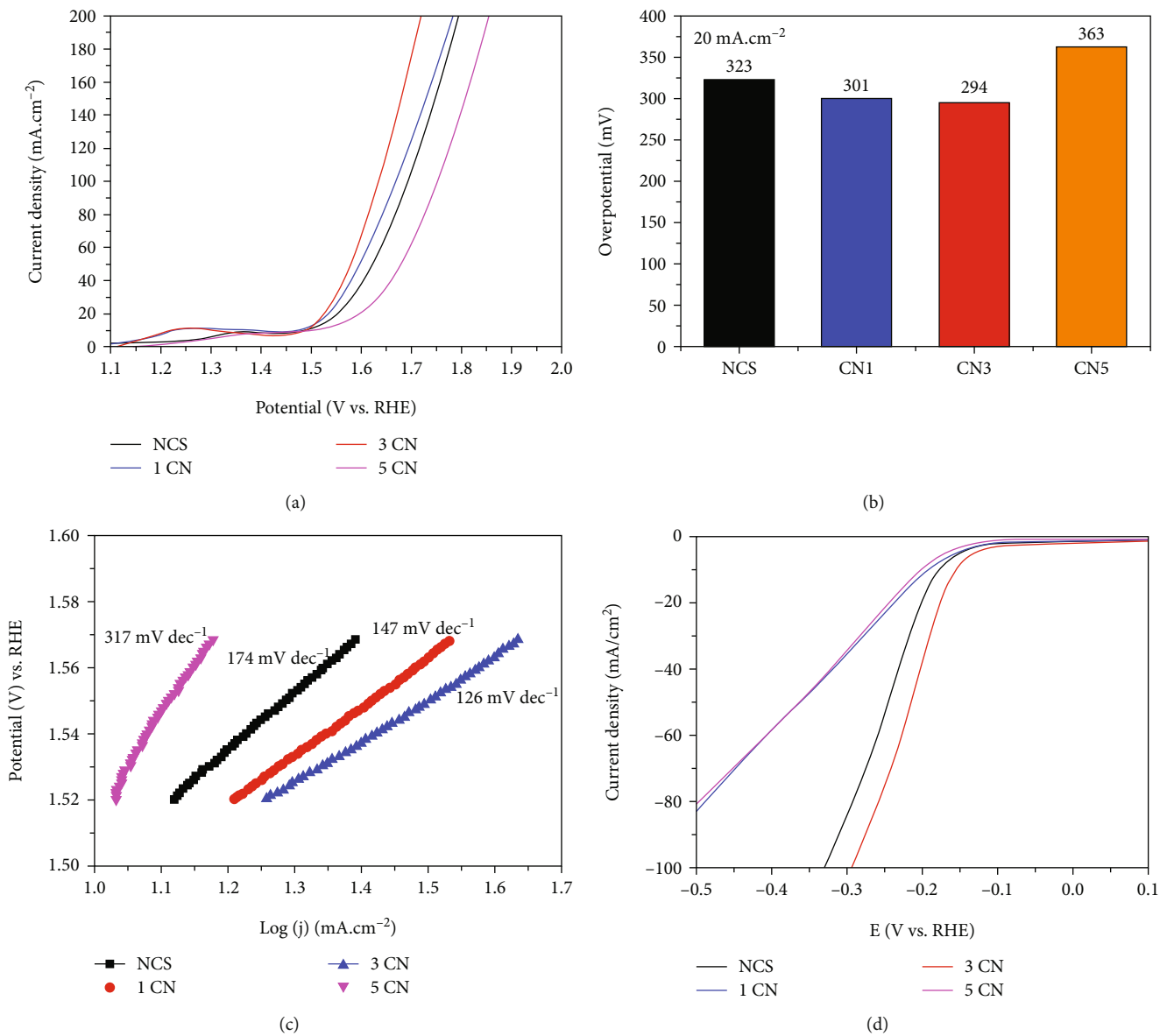


FIGURE 8: Continued.

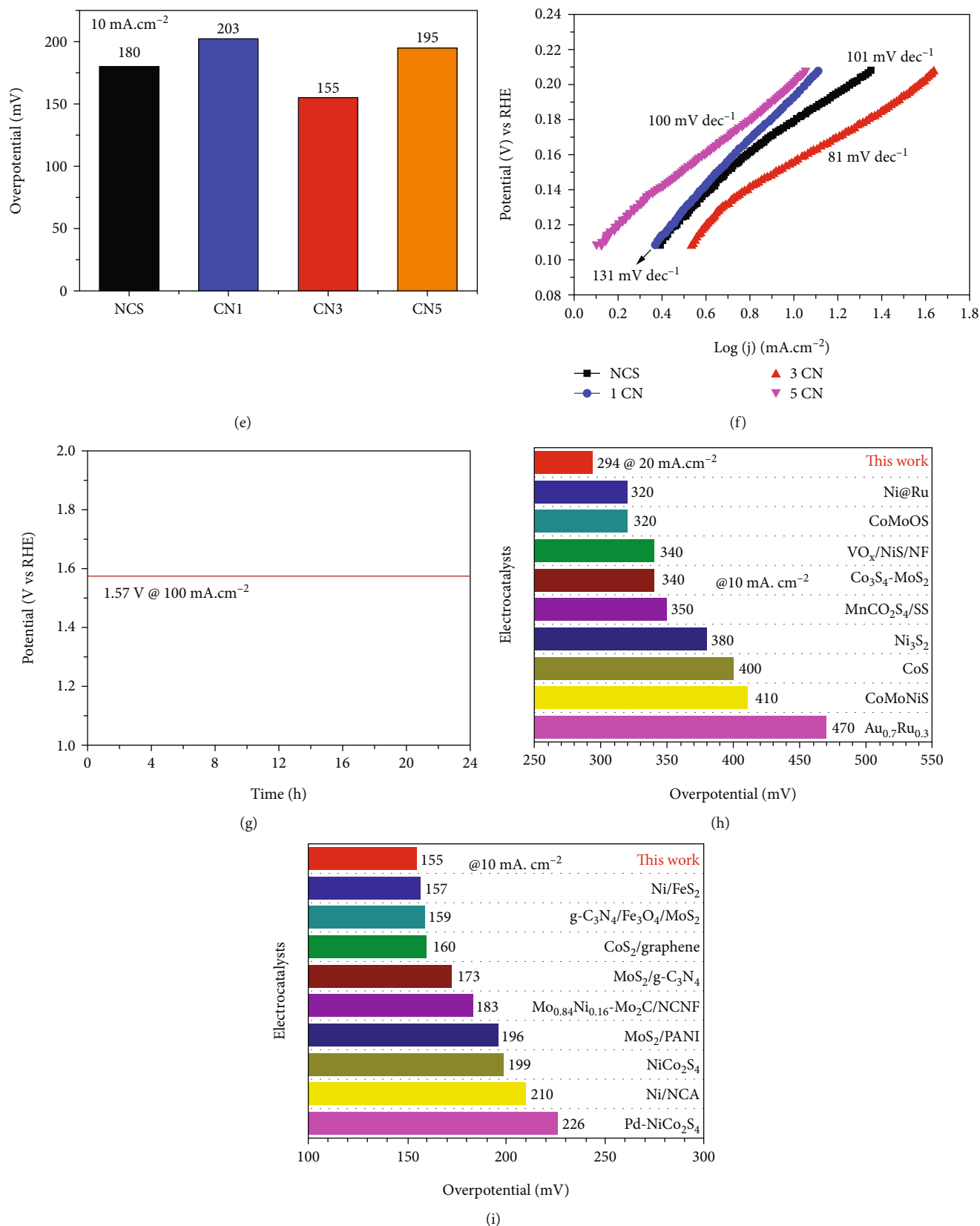


FIGURE 8: (a–c) OER polarization curves corresponding to Tafel plots and OER overpotential values of NCS aerogel and NCS/CN composite aerogels (1CN, 3CN, and 5CN) composite aerogels. (d–f) HER polarization curves corresponding to Tafel plots and HER overpotential values for NCS aerogel and NCS/CN composite aerogels (1CN, 3CN, and 5CN) composite aerogels. (g) OER potential stability of 3CN aerogel at a 100 mA.cm⁻² current density. (h, i) Comparison of OER and HER overpotentials with reported electrocatalysts, respectively.

MOF [89], show better HER and OER overpotentials compare with the present approach. The present approach lacks in the heterointerface engineering or hybridization, which can improve the supercapacitor as well as HER/OER performances of electrocatalyst by strong interaction. Therefore, the future work will be designed to enhance the performance of aerogel catalyst using heterointerface or hybridization engineering, decoration of layered double hydroxides [90], and oxygen functionalization [5], and the density functional theory will be used to demonstrate the interaction between NCS and CN composite interfaces. The present 3D aerogel design provides a new in situ sol-gel process to develop 0D and 2D assembled aerogels applicable in energy storage and conversion systems.

4. Conclusions

A new nanosandwich-like 2D CN nanosheet-assembled 3D macroporous multifunctional composite aerogels supported by NCS aerogel were synthesized using a simple in situ sol-gel self-assembly process. The synthesized aerogels exhibited hierarchically porous nanosandwich assembly with SSA of about $82 \text{ m}^2 \cdot \text{g}^{-1}$, which improves the electrochemical performance of these nanocomposite catalysts for energy storage and conversion. The NCS/CN composite aerogel electrode achieved a specific capacitance of $1083 \text{ F} \cdot \text{g}^{-1}$ at $5 \text{ mA} \cdot \text{cm}^{-2}$ with a remarkable stability of 87% over 10,000 cycles, better than pristine NCS aerogels (~62%). The fabricated 3% CN/NCS//AC ASC device achieved a specific capacitance of $137 \text{ F} \cdot \text{g}^{-1}$ at a 2 mA current for a stable 1.5 V potential window. This ASC further provides a maximum energy density of $43 \text{ Wh} \cdot \text{kg}^{-1}$ and power density of $86.66 \text{ W} \cdot \text{kg}^{-1}$ with an electrochemical stability of about 97% over 10,000 cycles. In addition, the CN/NCS nanocomposite aerogels unveiled comparable OER and HER enactment in an alkaline medium, achieving a minimum overpotential of 294 and 155 mV and Tafel slope value of 126 and $81 \text{ mV} \cdot \text{dec}^{-1}$, respectively. The present synthesis approach provides a new method to assemble 0D@2D nanomaterials for future energy storage and conversion applications.

Data Availability

Data will be made available on request.

Conflicts of Interest

The authors declare that they have no known competing financial interests or personal relationships that could appear to influence the work reported in this paper.

Authors' Contributions

Vinayak G. Parale and Younghun Kim were responsible for the conceptualization, writing—original draft, and formal analysis. Varsha D. Phadtare, Taehee Kim, Haryeong Choi, and Umakant M. Patil were responsible for the data curation, formal analysis, and investigation. Hyung-Ho Park

was responsible for the supervision and project administration. Vinayak G. Parale and Younghun Kim contributed equally to this work.

Acknowledgments

This work was supported by the National Research Foundation of Korea (NRF) grant funded by the Korean government (MSIT, No. 2020R1A5A1019131).

Supplementary Materials

S1: synthesis of porous 2D CN nanosheets. S2: formulae. Figure S1: synthesis process with visible photos of sol, gel, and aerogels for (a) NCS and (b) CN composite aerogels. Figure S2: high-resolution XPS spectra for (a) C 1s, N 1s, and O 1s of CN nanosheets and (b) Ni 2p, Co 2p, and S 2p of NCS aerogel. Figure S3: TEM images for porous CN nanosheets (pores are shown in Figure S3 (c) by yellow lines). Figure S4: TEM images (a, b) and HRTEM image (c) for NCS aerogels (Figure S4 (c) shows the interplanar spacing for NCS aerogels). Figure S5: TEM images with different resolutions for NCS/CN nanocomposite aerogels (the $\text{g-C}_3\text{N}_4$ nanosheets supported by NCS aerogels are assembled by in situ sol-gel assembly in the presence of MSA). Table S1: EDS elemental ratio for 3CN composite aerogels. Table S2: BET surface area values for NCS, $\text{g-C}_3\text{N}_4$, and CN composite aerogels. Figure S6: CV profiles for (a) NCS, (b) 1CN, and (c) 5CN electrodes at different scan rates and GCD profiles (d) NCS, (e) 1CN, and (f) 5CN electrodes at different current density values. Table S3: specific capacitance and specific capacity values for CN nanocomposite aerogels. Figure S7: log of current density vs. scan rate plot. Figure S8: graph of the calculated contribution of pseudocapacitive (surface current) and battery type (bulk current) current density values at various scan rates for (a) NCS, (b) 1CN, and (c) 3CN nanocomposite aerogel electrodes. Figure S9: EIS fitted circuit for present composite aerogel electrodes. Table S4: EIS-fitted parameters of NCS/CN composite aerogels. Figure S10: GCD profiles for NCS/CN composite aerogel//AC ASC device at different potential windows. Table S5: comparative electrochemical performance for $\text{NiCo}_2\text{S}_4/\text{g-C}_3\text{N}_4$ composite aerogel supercapacitor electrode over reported electrode materials. Table S6: fabricated and recently reported ASC supercapacitor device electrochemical performances. Figure S11: electrochemical active surface area (ECSA) analysis of the CN nanocomposite aerogels: the CV curves of (a) NCS, (b) 1CN, (c) 3CN, and (d) 5CN aerogels at various scan rates in small potential range (1.04–1.24 V vs. RHE) and (e) their anodic current linear fit for C_{dl} values. Figure S12: HER potential stability of 3CN aerogel at a $100 \text{ mA} \cdot \text{cm}^{-2}$ current density. Figure S13: (a) OER and (b) HER linear sweep voltammetry polarization curves before and after 24 h stability test. Figure S14: (a) XRD, (b) EDAX, (c) FESEM, and (d) TEM for 3CN composite aerogel catalyst after 24 h OER stability test. Figure S15: (a) XRD, (b) EDAX, (c) FESEM, and (d) TEM for 3CN composite aerogel catalyst after 24 h HER stability test. (*Supplementary Materials*)

References

- [1] S. S. Shinde, J. Y. Jung, N. K. Wagh et al., "Ampere-hour-scale zinc-air pouch cells," *Nature Energy*, vol. 6, no. 6, pp. 592–604, 2021.
- [2] J. Mao, J. Iocozzia, J. Huang, K. Meng, Y. Lai, and Z. Lin, "Graphene aerogels for efficient energy storage and conversion," *Energy & Environmental Science*, vol. 11, no. 4, pp. 772–799, 2018.
- [3] H.-S. Jeong, D. Kim, S. Jee et al., "Colloidal quantum dot: organic ternary ink for efficient solution-processed hybrid solar cells," *International Journal of Energy Research*, vol. 2023, Article ID 4911750, 14 pages, 2023.
- [4] D. Acharya, I. Pathak, A. Muthurasu et al., "In situ transmogrification of nanoarchitected Fe-MOFs decorated porous carbon nanofibers into efficient positrode for asymmetric supercapacitor application," *Journal of Energy Storage*, vol. 63, article 106992, 2023.
- [5] R. M. Bhattarai, K. Chhetri, N. Le et al., "Oxygen functionalization-assisted anionic exchange toward unique construction of flower-like transition metal chalcogenide embedded carbon fabric for ultra-long life flexible energy storage and conversion," *Carbon Energy*, no. article e392, 2023.
- [6] D. Acharya, I. Pathak, B. Dahal et al., "Immoderate nanoarchitectures of bimetallic MOF derived Ni-Fe-O/NPC on porous carbon nanofibers as freestanding electrode for asymmetric supercapacitors," *Carbon*, vol. 201, pp. 12–23, 2023.
- [7] A. R. Mule, D. Narsimulu, A. K. Kakarla, B. Ramulu, and J. S. Yu, "Unveiling hierarchical zinc-vanadium oxide composite microflakes as anode material for lithium-ion batteries," *International Journal of Energy Research*, vol. 2023, Article ID 1351959, 14 pages, 2023.
- [8] S. J. Marje, S. S. Pujari, S. A. Khalate et al., "Intercalation-type pseudocapacitive clustered nanoparticles of nickel-cobalt phosphate thin films synthesized via electrodeposition as cathode for high-performance hybrid supercapacitor devices," *Journal of Materials Chemistry A*, vol. 10, no. 20, pp. 11225–11237, 2022.
- [9] S. J. Marje, V. V. Patil, V. G. Parale et al., "Microsheets like nickel cobalt phosphate thin films as cathode for hybrid asymmetric solid-state supercapacitor: influence of nickel and cobalt ratio variation," *Chemical Engineering Journal*, vol. 429, article 132184, 2022.
- [10] J. Wu, "Understanding the electric double-layer structure, capacitance, and charging dynamics," *Capacitance, and Charging Dynamics, Chemical Reviews*, vol. 122, no. 12, pp. 10821–10859, 2022.
- [11] H. Wang, X. Liu, P. Niu, S. Wang, J. Shi, and L. Li, "Porous two-dimensional materials for photocatalytic and electrocatalytic applications," *Matter*, vol. 2, no. 6, pp. 1377–1413, 2020.
- [12] M. Ghaemmaghami and R. Mohammadi, "Carbon nitride as a new way to facilitate the next generation of carbon-based supercapacitors," *Sustainable Energy & Fuels*, vol. 3, no. 9, pp. 2176–2204, 2019.
- [13] Y. Wang, L. Liu, T. Ma, Y. Zhang, and H. Huang, "2D graphitic carbon nitride for energy conversion and storage," *Advanced Functional Materials*, vol. 31, no. 34, article 2102540, 2021.
- [14] Q. Yun, Y. Ge, B. Chen et al., "Hybridization of 2D nanomaterials with 3D graphene architectures for electrochemical energy storage and conversion," *Advanced Functional Materials*, vol. 32, no. 42, article 2202319, 2022.
- [15] T. Cui, Y.-P. Wang, T. Ye et al., "Engineering dual single-atom sites on 2D ultrathin N-doped carbon nanosheets attaining ultra-low-temperature zinc-air battery," *Angewandte Chemie International Edition*, vol. 61, no. 12, article e202115219, 2022.
- [16] X.-L. Pu, X.-C. Yang, S.-S. Liang, W. Wang, J.-T. Zhao, and Z.-J. Zhang, "Self-assembly of a g-C₃N₄-based 3D aerogel induced by N-modified carbon dots for enhanced photocatalytic hydrogen production," *Journal of Materials Chemistry A*, vol. 9, no. 39, pp. 22373–22379, 2021.
- [17] C. Rosso, G. Filippini, A. Criado, M. Meichionna, P. Fornasiero, and M. Prato, "Metal-free photocatalysis: two-dimensional nanomaterial connection toward advanced organic synthesis," *ACS Nano*, vol. 15, no. 3, pp. 3621–3630, 2021.
- [18] W. Niu and Y. Yang, "Graphitic carbon nitride for electrochemical energy conversion and storage," *ACS Energy Letters*, vol. 3, no. 11, pp. 2796–2815, 2018.
- [19] L. G. Ghanem, M. A. Hamza, M. M. Taha, and N. K. Allam, "Symmetric supercapacitor devices based on pristine g-C₃N₄ mesoporous nanosheets with exceptional stability and wide operating voltage window," *Journal of Energy Storage*, vol. 52, article 104850, 2022.
- [20] T. Li, J. Wu, L. Qiao et al., "Bimetallic Ni-Hf tellurides as an advanced electrocatalyst for overall water splitting with layered g-C₃N₄ modification," *Materials Today Energy*, vol. 26, article 101002, 2022.
- [21] V. D. Phadtare, V. G. Parale, T. Kim et al., "Ultrasonically dispersed ultrathin g-C₃N₄ nanosheet/BaBi₂Nb₂O₉ heterojunction photocatalysts for efficient photocatalytic degradation of organic pollutant," *Journal of Alloys and Compounds*, vol. 884, article 161037, 2021.
- [22] R. Ranjithkumar, P. Lakshmanan, P. Devendran, N. Nallamuthu, S. Sudhahar, and M. K. Kumar, "Investigations on effect of graphitic carbon nitride loading on the properties and electrochemical performance of g-C₃N₄/TiO₂ nanocomposites for energy storage device applications," *Materials Science in Semiconductor Processing*, vol. 121, article 105328, 2021.
- [23] K. C. Devarayapalli, K. Lee, H. B. Do et al., "Mesoporous g-C₃N₄ nanosheets interconnected with V₂O₅ nanobelts as electrode for coin-cell-type-asymmetric supercapacitor device," *Materials Today Energy*, vol. 21, article 100699, 2021.
- [24] R. R. Nallapureddy, M. R. Pallavolu, and S. W. Joo, "Construction of functionalized carbon nanofiber-g-C₃N₄ and TiO₂ spheres as a nanostructured hybrid electrode for high-performance supercapacitors," *Energy & Fuels*, vol. 35, no. 2, pp. 1796–1809, 2021.
- [25] V. G. Parale, T. Kim, A. M. Patil et al., "Construction of hierarchical nickel cobalt sulfide@manganese oxide nanorays@nanosheets-core-shell electrodes for high-performance electrochemical asymmetric supercapacitor," *International Journal of Energy Research*, vol. 46, no. 4, pp. 5250–5259, 2022.
- [26] J. Pu, F. Cui, S. Chu, T. Wang, E. Sheng, and Z. Wang, "Preparation and electrochemical characterization of hollow hexagonal NiCo₂S₄ nanoplates as pseudocapacitor materials," *ACS Sustainable Chemistry & Engineering*, vol. 2, no. 4, pp. 809–815, 2014.
- [27] Y. Zhang, M. Ma, J. Yang et al., "Shape-controlled synthesis of NiCo₂S₄ and their charge storage characteristics in supercapacitors," *Nanoscale*, vol. 6, no. 16, pp. 9824–9830, 2014.
- [28] M. B. Poudel, A. A. Kim, P. C. Lohani, D. J. Yoo, and H. J. Kim, "Assembling zinc cobalt hydroxide/ternary sulfides heterostructure and iron oxide nanorods on three-dimensional hollow porous carbon nanofiber as high energy density hybrid

- supercapacitor,” *Journal of Energy Storage*, vol. 60, article 106713, 2023.
- [29] K. Chhetri, T. Kim, D. Acharya et al., “Hollow carbon nanofibers with inside-outside decoration of Bi-metallic MOF derived Ni-Fe phosphides as electrode materials for asymmetric supercapacitors,” *Chemical Engineering Journal*, vol. 450, article 138363, 2022.
- [30] K. P. Gautam, D. Acharya, I. Bhatta et al., “Nickel oxide-incorporated polyaniline nanocomposites as an efficient electrode material for supercapacitor application,” *Inorganics*, vol. 10, no. 6, p. 86, 2022.
- [31] Q. Gao, X. Wang, Z. Shi et al., “Synthesis of porous NiCo₂S₄ aerogel for supercapacitor electrode and oxygen evolution reaction electrocatalyst,” *Chemical Engineering Journal*, vol. 331, pp. 185–193, 2018.
- [32] L. Xu, H. Wang, J. Gao, and X. Jin, “Electrochemical performance enhancement of flexible graphene supercapacitor electrodes by carbon dots modification and NiCo₂S₄ electrodeposition,” *Journal of Alloys and Compounds*, vol. 809, article 151802, 2019.
- [33] X. Wang, S. Wang, D. Su, S. Xu, S. Cao, and Y. Xiao, “Constructing a p-n heterojunction in 3D urchin-like CoNi_xS_y/g-C₃N₄ composite microsphere for high performance asymmetric supercapacitors,” *Journal of Alloys and Compounds*, vol. 902, article 163784, 2022.
- [34] J. Kavil, P. M. Anjana, P. Periyat, and R. B. Rakhi, “One-pot synthesis of g-C₃N₄/MnO₂ and g-C₃N₄/SnO₂ hybrid nanocomposites for supercapacitor applications,” *Sustainable Energy & Fuels*, vol. 2, no. 10, pp. 2244–2251, 2018.
- [35] Z. Li, L. Wu, L. Wang, A. Gu, and Q. Zhou, “Nickel cobalt sulfide nanosheets uniformly anchored on porous graphitic carbon nitride for supercapacitors with high cycling performance,” *Electrochimica Acta*, vol. 231, pp. 617–625, 2017.
- [36] S. Yesmin, I. Hussain, R. Dasgupta, and S. S. Dhar, “Two-dimensional tungsten oxide nanoflakes grafted over g-C₃N₄ as excellent electrode materials for hybrid supercapacitors,” *Journal of Energy Storage*, vol. 74, article 109383, 2023.
- [37] S. Wang, P. He, L. Jia et al., “Nanocoral-like composite of nickel selenide nanoparticles anchored on two-dimensional multi-layered graphitic carbon nitride: a highly efficient electrocatalyst for oxygen evolution reaction,” *Applied Catalysis B: Environmental*, vol. 243, pp. 463–469, 2019.
- [38] B. You and Y. Sun, “Innovative strategies for electrocatalytic water splitting,” *Accounts of Chemical Research*, vol. 51, no. 7, pp. 1571–1580, 2018.
- [39] X. Wang, Y. He, X. Han et al., “Engineering cobalt sulfide/oxide heterostructure with atomically mixed interfaces for synergistic electrocatalytic water splitting,” *Nano Research*, vol. 15, no. 2, pp. 1246–1253, 2022.
- [40] Y. Wu, X. Liu, D. Han et al., “Electron density modulation of NiCo₂S₄ nanowires by nitrogen incorporation for highly efficient hydrogen evolution catalysis,” *Nature Communications*, vol. 9, no. 1, p. 1425, 2018.
- [41] H. Su, S. Song, Y. Gao et al., “In situ electronic redistribution tuning of NiCo₂S₄ nanosheets for enhanced electrocatalysis,” *Advanced Functional Materials*, vol. 32, no. 14, article 2109731, 2022.
- [42] A. Rebekah, H. Amir, C. Viswanathan, and N. Ponpandian, “Enhanced bifunctional aspects of oxygen vacancy rich cation substituted MnCo₂O₄ intercalated with g-C₃N₄ as an oxygen evolution and supercapacitor electrode,” *International Journal of Hydrogen Energy*, vol. 48, no. 16, pp. 6384–6398, 2023.
- [43] K. Teng, W. Tang, R. Qi et al., “Nitrogen-deficient g-C₃N₄ compounded with NiCo₂S₄ (NiCo₂S₄@ND-CN) as a bifunctional electrocatalyst for boosting the activity of Li-O₂ batteries,” *Catalysis Today*, vol. 409, pp. 23–30, 2023.
- [44] M. B. Poudel, N. Logeshwaran, A. R. Kim, S. C. Karthikeyan, S. Vijayapradeep, and D. J. Yoo, “Integrated core-shell assembly of Ni₃S₂ nanowires and CoMoP nanosheets as highly efficient bifunctional electrocatalysts for overall water splitting,” *Journal of Alloys and Compounds*, vol. 960, article 170678, 2023.
- [45] R. Zahra, E. Pervaiz, M. M. Baig, and O. Rabi, “Three-dimensional hierarchical flowers-like cobalt-nickel sulfide constructed on graphitic carbon nitride: bifunctional non-noble electrocatalyst for overall water splitting,” *Electrochimica Acta*, vol. 418, article 140346, 2022.
- [46] U. Patil, S. C. Lee, S. Kulkarni et al., “Nanostructured pseudocapacitive materials decorated 3D graphene foam electrodes for next generation supercapacitors,” *Nanoscale*, vol. 7, no. 16, pp. 6999–7021, 2015.
- [47] B. Cai and A. Eychmüller, “Promoting electrocatalysis upon aerogels,” *Advanced Materials*, vol. 31, no. 31, article e1804881, 2019.
- [48] J. Yang, M. Ma, C. Sun, Y. Zhang, W. Huang, and X. Dong, “Hybrid NiCo₂S₄@MnO₂ heterostructures for high-performance supercapacitor electrodes,” *Journal of Materials Chemistry A*, vol. 3, no. 3, pp. 1258–1264, 2015.
- [49] J. Yang, Y. Chen, P. Xu, Y. Li, X. Jia, and H. Song, “Fabrication of compressible and underwater superoleophobic carbon/g-C₃N₄ aerogel for wastewater purification,” *Materials Letters*, vol. 254, pp. 210–213, 2019.
- [50] W. Guo, J. Wang, C. Fan et al., “Synthesis of carbon self-repairing porous g-C₃N₄ nanosheets/NiCo₂S₄ nanoparticles hybrid composite as high-performance electrode materials for supercapacitors,” *Electrochimica Acta*, vol. 253, pp. 68–77, 2017.
- [51] X. Renxin, H. Yanwen, Z. Wei, and C. Zhaohui, “A novel approach to estimate the state of charge for lithium-ion battery under different temperatures incorporating open circuit voltage online identification,” *Journal of Energy Storage*, vol. 67, article 107509, 2023.
- [52] L. Hu, J. Shi, Z. Peng, Z. Zheng, H. Dong, and T. Wang, “A high-density nickel-cobalt alloy embedded in nitrogen-doped carbon nanosheets for the hydrogen evolution reaction,” *Nanoscale*, vol. 14, no. 16, pp. 6202–6211, 2022.
- [53] L. Shen, J. Wang, G. Xu, H. Li, H. Dou, and X. Zhang, “NiCo₂S₄ nanosheets grown on nitrogen-doped carbon foams as an advanced electrode for supercapacitors,” *Advanced Energy Materials*, vol. 5, no. 3, article 1400977, 2015.
- [54] X. Ma, Q. Guo, J. Zhang et al., “[CH₃NH₃][M(HCOO)₃]-based 2D porous NiCo₂S₄ nanosheets for high-performance supercapacitors with high power densities,” *Chemical Engineering Journal*, vol. 437, article 135337, 2022.
- [55] A. Martínez-Lázaro, M. H. Rodríguez-Barajas, N. Rey-Raap et al., “Novel and high electrocatalytic activity aerogel Pd-TM (TM=Co, Ni, Fe),” *Materials Today Nano*, vol. 22, article 100308, 2023.
- [56] X. Wu, C. Ni, J. Man, X. Shen, S. Cui, and X. Chen, “A strategy to promote the ORR electrocatalytic activity by the novel engineering bunched three-dimensional Pd-Cu alloy aerogel,” *Chemical Engineering Journal*, vol. 454, article 140293, 2023.
- [57] C. Cheng, L. Mao, J. Shi et al., “NiCo₂O₄ nanosheets as a novel oxygen-evolution-reaction cocatalyst situated on the g-

- C₃N₄ photocatalyst for excellent overall water splitting,” *Journal of Materials Chemistry A*, vol. 9, no. 20, pp. 12299–12306, 2021.
- [58] N. S. Padalkar, S. V. Sadavar, R. B. Shinde et al., “Mesoporous nanohybrids of 2D Ni-Cr-layered double hydroxide nanosheets pillared with polyoxovanadate anions for high-performance hybrid supercapacitor,” *Advanced Materials Interfaces*, vol. 9, no. 1, article 2101216, 2022.
- [59] B. Pal, S. Yang, S. Ramesh, V. Thangadurai, and R. Jose, “Electrolyte selection for supercapacitive devices: a critical review,” *Nanoscale Advances*, vol. 1, no. 10, pp. 3807–3835, 2019.
- [60] R. Guo, L. Dang, Z. Liu, and Z. Lei, “Incorporation of electroactive NiCo₂S₄ and Fe₂O₃ into graphene aerogel for high-energy asymmetric supercapacitor,” *Colloids and Surfaces A: Physicochemical and Engineering Aspects*, vol. 602, article 125110, 2020.
- [61] W. Kong, C. Lu, W. Zhang, J. Pu, and Z. Wang, “Homogeneous core-shell NiCo₂S₄ nanostructures supported on nickel foam for supercapacitors,” *Journal of Materials Chemistry A*, vol. 3, no. 23, pp. 12452–12460, 2015.
- [62] X. Sun, H. Yang, H. Zhu et al., “Synthesis and enhanced supercapacitor performance of carbon self-doping graphitic carbon nitride/NiS electrode material,” *Journal of the American Ceramic Society*, vol. 104, no. 3, pp. 1554–1567, 2021.
- [63] S. Zhang, Y. Huang, J. Wang, X. Han, C. Chen, and X. Sun, “Ti₃C₂T_x/g-C₃N₄ heterostructure films with outstanding capacitance for flexible solid-state supercapacitors,” *Applied Surface Science*, vol. 599, article 154015, 2022.
- [64] G. Dong, H. Fan, K. Fu et al., “The evaluation of supercapacitive performance of novel g-C₃N₄/PPy nanocomposite electrode material with sandwich-like structure,” *Composites Part B: Engineering*, vol. 162, pp. 369–377, 2019.
- [65] H. Wang, M. Liang, C. Ma et al., “Novel dealloying-fabricated NiCo₂S₄ nanoparticles with excellent cycling performance for supercapacitors,” *Nanotechnology*, vol. 30, no. 23, article 235402, 2019.
- [66] B. Li, Z. Tian, H. Li, Z. Yang, Y. Wang, and X. Wang, “Self-supporting graphene aerogel electrode intensified by NiCo₂S₄ nanoparticles for asymmetric supercapacitor,” *Electrochimica Acta*, vol. 314, pp. 32–39, 2019.
- [67] M. R. Kandel, U. N. Pan, P. P. Dhakal et al., “Unique heterointerface engineering of Ni₂P–MnP nanosheets coupled Co₂P nanoflowers as hierarchical dual-functional electrocatalyst for highly proficient overall water-splitting,” *Applied Catalysis B: Environmental*, vol. 331, article 122680, 2023.
- [68] Z. Chen, W. Deng, D. Li et al., “Construction of CoNiS₂-g-C₃N₄ nanosheets with high exposed conductive interface for boosting oxygen evolution reaction,” *Journal of Alloys and Compounds*, vol. 887, article 161346, 2021.
- [69] G. He, M. Qiao, W. Li et al., “S, N-Co-doped graphene-nickel cobalt sulfide aerogel: improved energy storage and electrocatalytic performance,” *Advanced Science*, vol. 4, no. 1, article 1600214, 2017.
- [70] T. Wang, C. Li, X. Liao et al., “Fe-doped Co₉S₈@CoO aerogel with core-shell nanostructures for boosted oxygen evolution reaction,” *International Journal of Hydrogen Energy*, vol. 47, no. 49, pp. 21182–21190, 2022.
- [71] Y. Lv, S. Duan, Y. Zhu, P. Yin, and R. Wang, “Enhanced OER performances of Au@NiCo₂S₄ core-shell heterostructure,” *Nanomaterials*, vol. 10, no. 4, p. 611, 2020.
- [72] Z. Wang, J. Li, S. Liu, G. Shao, and X. Zhao, “A covalent organic framework/graphene aerogel electrocatalyst for enhanced overall water splitting,” *Nanoscale*, vol. 14, no. 45, pp. 16944–16951, 2022.
- [73] Y. Gu, S. Chen, J. Ren et al., “Electronic structure tuning in Ni₃FeN/r-GO aerogel toward bifunctional electrocatalyst for overall water splitting,” *ACS Nano*, vol. 12, no. 1, pp. 245–253, 2018.
- [74] J. Li, Q. Zhuang, P. Xu, D. Zhang, L. Wei, and D. Yuan, “Three-dimensional lily-like CoNi₂S₄ as an advanced bifunctional electrocatalyst for hydrogen and oxygen evolution reaction,” *Chinese Journal of Catalysis*, vol. 39, no. 8, pp. 1403–1410, 2018.
- [75] Y. Guo, J. Tang, H. Qian, Z. Wang, and Y. Yamauchi, “One-pot synthesis of zeolitic imidazolate framework 67-derived hollow Co₃S₄@MoS₂ heterostructures as efficient bifunctional catalysts,” *Chemistry of Materials*, vol. 29, no. 13, pp. 5566–5573, 2017.
- [76] W. Wu, Y. Wu, D. Zheng, K. Wang, and Z. Tang, “Ni@Ru core-shell nanoparticles on flower-like carbon nanosheets for hydrogen evolution reaction at all-pH values, oxygen evolution reaction and overall water splitting in alkaline solution,” *Electrochimica Acta*, vol. 320, article 134568, 2019.
- [77] S. Park, N. Utsch, M. Carmo, M. Shviro, and D. Stolten, “Iridium-nickel nanoparticle-based aerogels for oxygen evolution reaction,” *ACS Applied Nano Materials*, vol. 5, no. 12, pp. 18060–18069, 2022.
- [78] W. Moschkowitsch, N. Zion, H. C. Honig, N. Levy, D. A. Cullen, and L. Elbaz, “Mixed-metal nickel-iron oxide aerogels for oxygen evolution reaction,” *ACS Catalysis*, vol. 12, no. 19, pp. 12162–12169, 2022.
- [79] M. Jiang, Y. Zou, F. Xu et al., “Synthesis of g-C₃N₄/Fe₃O₄/MoS₂ composites for efficient hydrogen evolution reaction,” *Journal of Alloys and Compounds*, vol. 906, article 164265, 2022.
- [80] R. C. Pawar, S. Kang, H. Khan, H. Han, and C. S. Lee, “Study of multi-faceted CoS₂ introduced graphene aerogel hybrids via chemical approach for an effective electrocatalytic water splitting,” *Current Applied Physics*, vol. 32, pp. 78–85, 2021.
- [81] S. Geng, W. Yang, and Y. S. Yu, “Building MoS₂/S-doped g-C₃N₄ layered heterojunction electrocatalysts for efficient hydrogen evolution reaction,” *Journal of Catalysis*, vol. 375, pp. 441–447, 2019.
- [82] S. Das, R. Ghosh, P. Routh et al., “Conductive MoS₂ quantum dot/polyaniline aerogel for enhanced electrocatalytic hydrogen evolution and photoresponse properties,” *ACS Applied Nano Materials*, vol. 1, no. 5, pp. 2306–2316, 2018.
- [83] P. Shanmugam, A. P. Murthy, J. Theerthagiri et al., “Robust bifunctional catalytic activities of N-doped carbon aerogel-nickel composites for electrocatalytic hydrogen evolution and hydrogenation of nitrocompounds,” *International Journal of Hydrogen Energy*, vol. 44, no. 26, pp. 13334–13344, 2019.
- [84] G. Sheng, J. Chen, Y. Li et al., “Flowerlike NiCo₂S₄ hollow microspheres with mesoporous nanoshells support Pd nanoparticles for enhanced hydrogen evolution reaction electrocatalysis in both acidic and alkaline conditions,” *ACS Applied Materials & Interfaces*, vol. 10, no. 26, pp. 22248–22256, 2018.
- [85] W. Zhao, X. Lu, M. Selvaraj et al., “MXP (M = Co/Ni)@carbon core-shell nanoparticles embedded in 3D cross-linked graphene aerogel derived from seaweed biomass for hydrogen evolution reaction,” *Nanoscale*, vol. 10, no. 20, pp. 9698–9706, 2018.

- [86] S. Tang, X. Wang, Y. Zhang, M. Courté, H. J. Fan, and D. Fichou, "Combining Co_3S_4 and $\text{Ni}:\text{Co}_3\text{S}_4$ nanowires as efficient catalysts for overall water splitting: an experimental and theoretical study," *Nanoscale*, vol. 11, no. 5, pp. 2202–2210, 2019.
- [87] C. Lin, Z. Gao, and J. Jin, "Boosting alkaline hydrogen evolution activity with Ni-doped MoS_2 /reduced graphene oxide hybrid aerogel," *ChemSusChem*, vol. 12, no. 2, pp. 457–466, 2019.
- [88] M. R. Kandel, U. N. Pan, D. R. Paudel, P. P. Dhakal, N. H. Kim, and J. H. Lee, "Hybridized bimetallic phosphides of Ni–Mo, co–Mo, and co–Ni in a single ultrathin-3D-nanosheets for efficient HER and OER in alkaline media," *Composites Part B: Engineering*, vol. 239, article 109992, 2022.
- [89] K. Chhetri, A. Muthurasu, B. Dahal et al., "Engineering the abundant heterointerfaces of integrated bimetallic sulfide-coupled 2D MOF-derived mesoporous CoS_2 nanoarray hybrids for electrocatalytic water splitting," *Materials Today Nano*, vol. 17, article 100146, 2022.
- [90] M. Pourshahmir, S. Ghasemi, and S. R. Hosseini, "Nickel-cobalt layered double hydroxide/ NiCo_2S_4 /g- C_3N_4 nanohybrid for high performance asymmetric supercapacitor," *International Journal of Hydrogen Energy*, vol. 48, no. 22, pp. 8127–8143, 2023.